Chemical Engineering Journal 525 (2025) 169095

Contents lists available at ScienceDirect

Chemical Engineering Journal

journal homepage: www.elsevier.com/locate/cej

Olivine dissolution kinetics at elevated temperatures and pressures

Qiaoyun Chen, J.P. Martin Trusler *

Department of Chemical Engineering, Imperial College London, South Kensington Campus, London, SW7 2AZ, UK

ARTICLE INFO

Keywords:
Olivine
Carbon mineralization
Dissolution
Kinetics
High temperatures
Passivation layers
Mass transfer effect

ABSTRACT

Experimental and modelling studies of the dissolution kinetics and surface chemistry of olivine in CO_2-saturated water at elevated temperatures and CO_2 pressures are reported. The apparent initial dissolution rates of olivine are reported at temperatures between 373 and 473 K and at pressures between 7.7 and 15.6 MPa. The influence of mass transfer effects on olivine dissolution and the formation of passivation layers were studied, and the minimum stirring speed at which mass transfer resistance was effectively eliminated was determined. The optimum temperature for olivine dissolution in the long term was determined to be approximately 423 K. This study provides the first data for olivine dissolution rates at temperatures above 423 K. The initial olivine dissolution rates did not show a monotonic increasing trend with the increase of temperature due to the formation of various passivation layers on the olivine particle surfaces at different temperatures. A simple model, dependent upon temperature and the activity of H^+, was developed to represent the experimental data. This model is generally applicable under similar temperature and pressure conditions, and when the same type of passivation layer is present. Based on the proposed model, the *PHREEQC* geochemical simulator was used to predict the saturation indices of Fe_2O_3 (hematite), FeO(OH) (goethite), $Fe(OH)_3$ (ferric hydroxide) and SiO_2 (both quartz and amorphous silica). The *p*H and elemental concentrations were also predicted and these calculations served to partially rationalize the experimental results.

1. Introduction

Carbon mineralization is one of the promising methods for lasting and secure carbon storage, mitigating the rising atmospheric CO_2 concentration and helping to address climate change [1]. In-situ and ex-situ carbon mineralization are the two pathways of this method [1]. In-situ carbon mineralization serves as one of the four trapping mechanisms of geological carbon storage (GCS): structural, capillary, solubility and mineralization trapping [2]. Among these trapping mechanisms, mineralization may offer the most permanent form of GCS, as converting CO_2 into solid carbonate rock effectively eliminates the possibility of leakage. For in-situ mineralization, mafic and ultramafic rocks first dissolve in CO_2-acidified water to release divalent cations such as Mg^{2+}, Fe^{2+} and Ca^{2+} which subsequently react with HCO_3^- and/or CO_3^{2-} at higher *p*H to form stable carbonate precipitates. One of the main rate-limiting steps for in-situ carbon mineralization is the dissolution of these silicate rocks, which serve as source rocks to produce cations for carbonation. The dissolution kinetics of these source rocks is crucial for understanding the reactions in CO_2-brine-mineral systems and predicting the extent and rate of carbon mineralization.

For ex-situ carbon mineralization, CO_2 is converted into stable carbonate minerals through engineered processes conducted above ground [1,3]. Common feedstocks for this approach include mine tailings, fly ash, reactive rocks, and steel slags [1,3–5]. One advantage of ex-situ mineralization is that the resulting inorganic carbonate minerals and other potential by-products might be recovered and utilized as valuable materials [1,6–9]. As with in-situ mineralization, silicates are suitable source rocks for ex-situ carbon mineralization.

Olivine, a common mineral found in mafic and ultramafic rocks, was chosen as the focus of this study because of its high reactivity and abundance. Olivine is a magnesium-iron silicate with the general chemical formula $(Mg_{2-n}Fe_n)SiO_4$ for $0 \leq n \leq 2$. It can be used for both in-situ and ex-situ pathways [10,11]. Mineralization of CO_2 begins with its dissolution in and reaction with the aqueous medium to form carbonic acid, bicarbonate ions or carbonate ions, depending upon the *p*H, according to the following reactions:

$$CO_2(g) = CO_2(aq) \quad (1)$$

* Corresponding author.
E-mail address: m.trusler@imperial.ac.uk (J.P.M. Trusler).

https://doi.org/10.1016/j.cej.2025.169095
Received 4 July 2025; Received in revised form 24 September 2025; Accepted 28 September 2025
Available online 3 October 2025
1385-8947/© 2025 The Authors. Published by Elsevier B.V. This is an open access article under the CC BY-NC-ND license (http://creativecommons.org/licenses/by-nc-nd/4.0/).

$$CO_2(aq) + H_2O(aq) = H_2CO_3(aq) = HCO_3^-(aq) + H^+(aq) = CO_3^{2-}(aq) + 2H^+(aq) \quad (2)$$

Here, $CO_2(aq)$ or $H_2CO_3(aq)$ are the primary species at acid conditions, while HCO_3^- dominates at neutral to slightly alkaline conditions, and CO_3^{2-} dominates at strongly alkaline conditions [12–15].

The dissolution of source rock can be illustrated by reference to the Mg-rich end member of the olivine group, forsterite (Fo_{100}), as follows:

$$Mg_2SiO_4(s) + 4H^+(aq) = 2Mg^{2+}(aq) + H_4SiO_4(aq). \quad (3)$$

Finally, the precipitation of $MgCO_3$ under acid to slightly alkaline conditions follows mainly the reaction

$$Mg^{2+}(aq) + HCO_3^-(aq) = MgCO_3(s) + H^+(aq), \quad (4)$$

whereas under strongly alkaline conditions, $MgCO_3$ is precipitated according to the reaction

$$Mg^{2+}(aq) + CO_3^{2-}(aq) = MgCO_3(s). \quad (5)$$

Overall, the net reaction mineralization reaction with forsterite as the source rock is:

$$2CO_2(aq) + 2H_2O(aq) + Mg_2SiO_4(s) = 2MgCO_3(s) + H_4SiO_4(aq). \quad (6)$$

The dissolution of olivine follows a path similar to reaction (3) and the kinetics of this process under different conditions have been studied over several decades. Chen and Brantley [16], Rosso and Rimstidt [17] and Oelkers [18] studied the dissolution kinetics of olivine at temperatures between 298.15 and 338.15 K, at low *p*H and in the absence of CO_2. Wogelius and Walther [19], Golubev et al. [20] and Pokrovsky and Schott [21] studied the dissolution kinetics of olivine at CO_2 pressures less than 0.1 MPa, at a temperature of 298.15 K, and at *p*H ranging from 1 to 12. Giammar et al. [22], Wang and Giammar [23], Hänchen et al. [24], Prigiobbe et al. [25,26], Johnson et al. [11] and Daval et al. [27] studied the dissolution kinetics of olivine at higher temperatures from 303.15 to 423.15 K and at higher CO_2 pressures up to 25 MPa.

In the literature, a temperature and/or *p*H dependent kinetic model was usually adopted to represent the olivine dissolution rates [16–19,24,25,28,29]. Considering both factors, the general model is given by

$$r = A\exp(-E_a/RT)a_{H^+}^n. \quad (7)$$

Here r is dissolution rate per unit surface area, A is a pre-exponential factor, E_a is activation energy, R is the gas constant, T is thermodynamic temperature, a_{H^+} is the activity of H^+, and n is the reaction order with respect to H^+.

Other factors that have been studied include the effects of additional components, such as potassium hydrogen phthalate [29], ascorbic acid [29], oxalate [26], citrate [26], aluminium ions [16], variation of salinity [23,25], and the formation of secondary phases such as silica passivation layers [27,30], and ferric iron-rich phases [16,29]. Wogelius and Walther [29] concluded that the effects of organic ligand were more pronounced under near neutral conditions than under acidic conditions at 298.15 K. Prigiobbe and Mazzotti [26] found that the presence of sodium oxalate and sodium citrate enhanced olivine dissolution rates at 363.15 and 393.15 K and at *p*H between 2 and 7, likely because the oxalate and citrate ions, which were the main species in the *p*H ranges studied, can form surface complexes which facilitated the breakdown of protonated silica tetrahedra. Chen and Brantley [16] found that olivine dissolution rates were almost independent of the concentration of aluminium (III) ions up to 0.4 mmol·l^{-1} at 338.15 K and *p*H of 2.95. This was likely because the potential adsorption of aluminium onto the olivine surface did not result in the formation of stable crosslinks between isolated silica tetrahedra [16]. Wang and Giammar [23] found that NaCl accelerated olivine dissolution rates at 373.15 K and CO_2 pressure of 10 MPa, potentially by preventing the formation of a silica-rich passivation layer on the olivine surface. On the other hand, Prigiobbe et al. [25] concluded that the presence of NaCl and $NaNO_3$ influenced olivine dissolution rates through their effects on *p*H at 393.15 K and $3 \leq pH \leq 8$.

Daval et al. [27] found that the formation of amorphous silica layers on the olivine surface decreased dissolution rates at 363.15 K and high CO_2 pressures up to 25 MPa. Saleh et al. [30] observed the formation of silica precipitates in CO_2-rich systems, whereas no silica precipitation occurred in water-rich systems at 363.15 and 423.15 K and at CO_2 pressures between 2 and 9 MPa. Chen and Brantley [16] inferred that instead of the formation of ferric iron rich-layer, the olivine surface may have been oxidized in their open-air experiments, leading to a decreased dissolution rate. Wogelius and Walther [29] concluded that the presence of a ferric iron-rich layer on the olivine surface either by precipitation or in-situ oxidation of ferrous iron could ultimately reduce the dissolution rate, based on their experiments with fayalite, the iron-rich end member of the olivine group.

To the best of our knowledge, there have been no studies of the kinetics of olivine dissolution at temperatures above 423 K. We identified lack of higher-temperature data as a significant research gap. For example, CO_2-saturated water was injected into a hydrothermally-altered basalt formation at depths of more than 1300 m below the surface and at temperatures above 523 K for carbon mineralization in the CarbFix2 project [31,32]. Additionally, the influence of mass transfer effects on olivine dissolution kinetics has not been investigated, despite its importance for informing the design of ex-situ carbon mineralization projects and enhancing our understanding of in-situ carbon mineralization processes.

Therefore, the objectives of this study were as follows.

- To investigate the reaction behaviour, mechanisms, and kinetics for olivine dissolution in CO_2-saturated water at temperatures up to 473 K and at CO_2 pressures up to 15.6 MPa;
- To study the influences of mass transfer resistance and different types of passivation layers on olivine dissolution kinetics;
- To develop a simple model to correlate the experimental kinetic data as a function of temperature and the activity of H^+.

The following sections begin with a summary of the materials and experimental procedures, followed by the determination of the initial olivine dissolution rates. The Results and discussions section presents the influence of mass transfer effect on olivine dissolution rates, olivine dissolution kinetics and mechanistic behaviour, and the effects of temperature, CO_2 pressure, and passivation layer on olivine dissolution, along with modelling results. Finally, the Conclusions section highlights the key findings of this study.

2. Materials and measurement system

2.1. Materials and chemicals

The gem-quality olivine chips (3–7 mm) originating from Pakistan were purchased from UKGE limited. These olivine chips were highly crystalized and non-porous. They were first ground into powder using a planetary ball mill with zirconia grinding balls and jar, after which the powder was passed through two sieves with openings of 212 and 106 μm, respectively. The powder that passed through the first but not the second sieve was the selected fraction; this material was then washed in 2-proponal in an ultrasonic cleaner until the supernatant was clear. Finally, the cleaned particles were dried in an air oven at 333 K overnight. The Brunauer, Emmett and Teller (BET) method [33] was used to determine the specific surface area of the olivine particles. N_2 adsorption at 77 K was measured using the Autosorb iQ instrument from Quantachrome. In view of the non-porous nature of the material, a large sample of approximately 6.4 g was used to ensure sufficient total surface area in the cell for reliable results. The specific surface area S was determined to be 0.137 m^2·g^{-1} with a standard uncertainty $u(S)$ =

$0.007\ m^2 \cdot g^{-1}$.

The olivine particles were analysed for chemical composition by X-ray photoelectron spectroscopy (XPS) and for structure by X-ray diffraction (XRD). A Thermo Scientific K-Alpha X-ray XPS system and a PANalytical X'pert Pro XRD system were used. The atomic percentages of different orbitals for olivine determined by XPS analysis are presented in Table A.1 (Supplementary information SI A). The XPS peak fitting is given in Supplementary information SI B. The XRD pattern with the best matched reference pattern from the database is shown in Fig. A.1 (Supplementary information SI A). The sum chemical formula was determined to be $(Mg_{1.8}, Fe_{0.2})SiO_4$. Scanning electron microscopy (SEM) images of an olivine chip as received, and of the olivine particles obtained after milling, sieving and ultrasonic cleaning, are shown in Figs. A.2 and A.3, respectively. A ZEISS Sigma 300 SEM coupled with a Bruker XFlash 6160 EDX detector was used.

The chemicals used in this study are listed in Table 1.

2.2. Measurement system

The measurement system consisted of a batch reactor system [34] fitted with an auto-sampling system, as shown in Fig. 1.

The batch reactor system consisted of two vessels (model 4545) manufactured by the Parr Instrument Company. The material of the wetted parts of the whole system was Hastelloy C276 to be resistant to corrosion. The reactors were sealed by PTFE gaskets along with split ring halves and compression bolts. A rupture-disc safety device was fitted to the reactor head for pressure release purpose. Each reactor vessel was heated by an electric heating jacket, which also served as insulation. The impeller and stirrer shaft assembly were driven indirectly by a variable speed electric motor with a magnetic drive coupling. The 5-blade impeller had an outer diameter of 45 mm, a hub diameter of 19 mm, a bore diameter of 8 mm and a height of 16.5 mm. The blade (12.5 mm × 9.8 mm × 1.5 mm) had an inclination angle of 45°. The standard uncertainty of the stirring angular velocity was $0.6\ s^{-1}$. A 1/8″ diameter type J thermocouple probe was inserted into a thermowell to measure the temperature within each vessel. The resolution of the temperature measurements was 0.01 K and the estimated standard uncertainty was 1 K. The pressure in each reactor was measured with pressure transducers connected to the reactor lids. These had a full-scale reading of 51.7 MPa and a standard uncertainty of 0.07 MPa.

Each reactor vessel was equipped with a Parr 4848 PID controller to control the temperature and stirring rate. These controllers monitored the pressure of the vessels, and provided safety cut-out protection when one of the variables exceeded the safety values. The controllers were interfaced (via RS 485 interfaces) with a computer running *SpecView* software, through which the temperatures, pressures and stirring rates of the reactors were logged.

The two vessels had a maximum capacity of 600 ml, an inner diameter of 82.3 mm and an internal depth of 121.3 mm. These vessels were rated for a maximum operating pressure of 39.3 MPa and a maximum operating temperature of 505 K. The liquid in reactor 1 could be transferred to reactor 2 via a transfer tube (17 in Fig. 1) by opening valve V-8. The transfer tube was heated by electric heating cable and insulated with silicone-rubber sponge. The CO_2 was injected from a syringe pump (Teledyne Isco model 260 D) fitted with a cooling jacket operating with a chiller to ensure that the CO_2 inside the pump was liquefied.

A customized auto-sampling system was developed. As shown in Fig. 1, it consisted of a fraction collector, two six-port valves (with valve body made of Nitronic 60) fitted with electric actuators, a N_2 cylinder, an air-actuated on/off valve with needle made of Cobalt alloy, a syringe pump, a three-port solenoid valve, a two-port solenoid valve, a solvent waste bottle and a sample waste bottle. The air-actuated on/off valve was controlled by the three-port solenoid valve and N_2 supply, while the two solenoid valves were actuated via a Keysight model 34970A Data Acquisition/Switch unit. A filter with a PEEK-encased titanium frit (pore size 0.5 μm, frit OD 4.6 mm) fully exposed to the particle-liquid slurry, was connected to the end of connecting tubing 18 within vessel 2 to filter solids when taking liquid samples. The calibration of the volumes of sample loop 19 and solvent loop 21, the detailed operation procedure of the auto-sampling system, the validation of the auto-sampling system, and the standard operating procedure are given in Supplementary information SI C.

To summarize the standard operating procedure, CO_2-saturated water was transferred from reactor 1 to reactor 2, which contained olivine particles, thereby initiating the reaction in the olivine-water-CO_2 system under the CO_2 atmosphere. During the reaction, liquid samples were periodically collected from reactor 2 via the auto-sampling system. The liquid samples were analysed by inductive coupled plasma mass spectrometry (ICP-MS) to determine the concentrations of Mg, ^{28}Si and Fe, and/or inductively coupled plasma optical emission spectroscopy (ICP-OES) to determine the concentrations of Mg, Si and Fe. In this study, an Agilent model 7900 ICP-MS and a Thermo Scientific iCAP 6000 Series ICP-OES were used. The recovered reacted olivine particles were analysed by XPS and time-of-flight secondary ion mass spectrometry (ToF-SIMS). For the latter, an IONTOF TOF.SIMS 5 was used.

3. Determination of initial olivine dissolution rate

The initial mineral dissolution rate r was determined by

$$r = (dc/dt)(V/S_t). \tag{8}$$

Here c is the element concentration in the solution, t is the reaction time, V is the volume of the solution, and S_t is the total exposure mineral area, determined by the mass m of the mineral powder and the specific area S of the powder.

To obtain the stoichiometric dissolution rate of olivine, the chemical formula of olivine needs to be considered, so c was divided by 1.8 when using the Mg concentration for the dissolution rate calculation. The olivine dissolution rate r_{Oliv} was taken an average of the stoichiometric dissolution rates calculated by Mg and Si ($r_{stoi,Mg}$ and $r_{stoi,Si}$), and is given by

$$r_{Oliv} = \frac{1}{2}\left(r_{stoi,Mg} + r_{stoi,Si}\right) = \frac{1}{2}\left(r_{Mg}/1.8 + r_{Si}\right), \tag{9}$$

where r_{Mg} and r_{Si} are the released rate of Mg and Si.

Under certain conditions the reaction reached equilibrium within minutes, so the dissolution rate at the beginning of the reaction was quantified across all experimental conditions. Despite being an initial

Table 1
Specification of chemicals. Here x is mole fraction, ρ_e is electrical resistivity at $T = 298$ K and w is mass fraction.

Chemical	Purity as stated by supplier	CAS number	Supplier	Additional purification
CO_2	$x \geq 0.99995$	124-38-9	BOC	None
H_2O	$\rho_e \geq 18.2$ MΩ·cm	7732-18-5	Produced in house	Degassed
HNO_3	$w \sim 0.69$	7697-37-2	Fisher Scientific	None
Fe_2O_3	$w \geq 0.99995$	1309-37-1	Sigma Aldrich	Calcination at 973 K overnight
Goethite	w(Fe): 0.3–0.63	20344-49-4	Sigma Aldrich	None

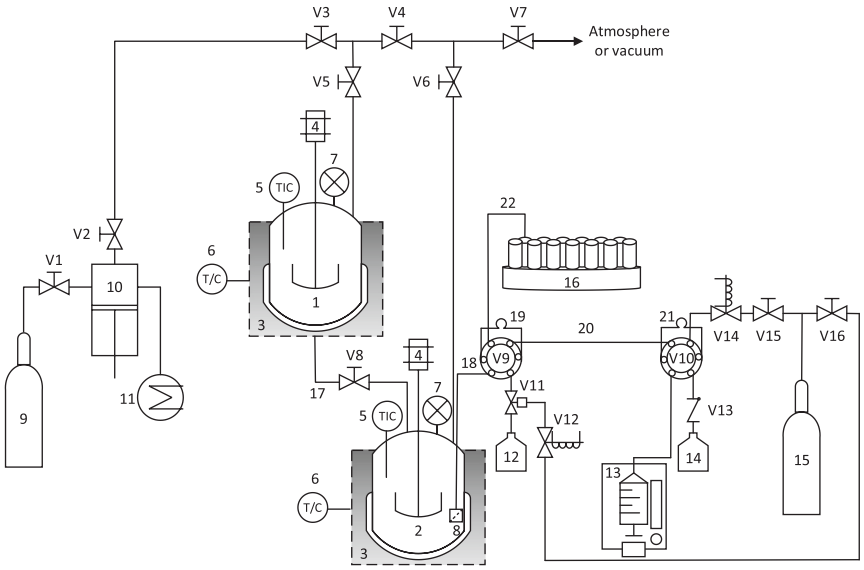


Fig. 1. Schematic of measurement system. 1, vessel 1; 2, vessel 2; 3, heater jacket; 4, stirring assembly; 5, 6, thermocouple; 7, pressure transducer; 8, filter; 9, CO_2 cylinder; 10, syringe pump; 11, chiller; 12, 14, waste bottle; 13, syringe pump for in-line solvent; 15, N_2 cylinder; 16, fraction collector; 17, transfer tubing between vessels 1 and 2; 18, connecting tubing between vessel 2 and auto-sampling system; 19, sample loop; 20, connecting tubing between two sampling valves; 21, solvent loop; 22, connecting tubing between fraction collector and sampling valves. V1–V8, V15, V16, manual valves; V9, V10, sampling valves; V11, on/off valve; V12, V14, solenoid valves; V13, check valve.

rate, the reported values still reflected the reaction process including the formation of passivation layers and their effects, over a period of time, in light of the calculation method. The apparent initial dissolution rates were determined based on the evolution of the concentrations of Mg and Si in a period of time, so any factor such as the formation of passivation layer affecting the dissolution of olivine and subsequently the concentrations of Mg and Si, consequently influenced the calculation of initial dissolution rates.

Additionally, it is worth mentioning that some fine dust from the olivine particles was observed when reactor 2 was opened after the experiment. This was probably formed by attrition at the high stirring speeds used in the experiment. Unfortunately, it was difficult to collect this tiny amount of fine dust for any analysis such as surface area analysis. Additionally, it was not possible to measure the surface area of the recovered reacted olivine particles accurately because only about 1 g of olivine particles were used in each experiment, which was too little for a sensitive BET measurement. Besides, the reaction itself was also likely to alter the surface area of the particles. However, because the initial dissolution rate was of interest in this study, the surface area of olivine particles was assumed remain unchanged at the early stage of reaction.

4. Results and discussions

Batch reaction experiments were conducted on olivine dissolution in CO_2-saturated water at pressures between 7.7 and 15.6 MPa and at temperatures between 373 and 473 K. For each experiment, between 275 and 340 ml of pure water was added to reactor 1 and about 1 g of olivine powder was added to reactor 2. Each reaction lasted for about 75 min, during which liquid samples were taken from reactor 2 via the auto-sampling system. A blank test without olivine powder was performed to assess the background level of Si, Mg and Fe produced by the measurement system, as shown in Supplementary information SI D.

Unfortunately, there was contamination with Si and Fe from both the auto-sampling system (which was the main contamination source) and the batch reactors themselves, because some wetted parts contain Fe and Si. A sample was always collected directly from reactor 2 using a pipettor after the reaction was finished and reactor 2 was opened. This sample did not pass through the auto-sampling system. Because this sample and the last sample that was collected by the auto-sampling system experienced almost the same reaction time, comparison of the concentrations of Mg, Si and Fe between these two samples allowed the amount of the contamination from the auto-sampling to be estimated.

Because the amount of Fe released from the olivine was smaller than or similar to the contamination from the system, the measured concentrations of Fe was not considered to be reliable even with correction, but the trend of the Fe concentration as a function of the reaction time showed different patterns at different conditions, providing useful information about the reaction. This will be discussed in the following sections. For Si, the amount that was released from the olivine was much higher than the contamination, so the results for this element were considered reliable after application of a correction based on the blank test.

4.1. Influence of mass transfer effect on olivine dissolution rates

Tests were carried out to determine the stirring speeds necessary to suspend the particles and to effectively eliminate mass transfer resistance. The angular velocities used in these experiments were 42, 73, 89, 105 and 120 s^{-1}. To observe the effects of stirring visually at various angular velocities, a transparent beaker with a size and shape similar to reactor 2 was used for an observation test performed at ambient conditions. In this test, the same amounts of olivine particles and water as in the actual experiment were used, and the angular velocity was set to the values of interest. At 42 s^{-1}, the particles remained stationary at the bottom, while the liquid was stirred homogeneously. At 73 and 89 s^{-1}, the particles were partially suspended while, at 105 and 120 s^{-1}, they were fully suspended in the liquid.

To determine the angular velocity of the stirrer at which the mass transfer effect was eliminated, a series of experiments at the highest temperature (473 K) and pressure (15.6 MPa) were conducted. The measured concentration profiles of Mg and Si, and the concentration ratio profiles between Mg and Si as a function of reaction time are shown in Fig. 3. The concentrations of Mg and Si were fitted as a function of time by the following equation

$$c = c_e[1 - \exp(-t/\tau)] + c_0. \quad (10)$$

Here, c is the concentration of Mg or Si, t is the reaction time, c_e is the

equilibrium concentration, τ is a reaction time constant, and c_0 is a constant introduced to represent either an initial background concentration or the possibility of some initial and very rapid reaction process that occurred before the first sample was collected. This will be discussed in the following sections.

To best represent the initial dissolution rate, data points from either the full reaction duration or the initial reaction period were fitted, and the resulting parameters were used. Based on Eqs. (8)–(10), the apparent initial olivine dissolution rates were determined. Although these represent initial reaction rates, the reported values still reflected the reaction process during the period in which the concentration profiles of Mg and Si were fitted. This was because the changes in Mg and Si concentration profiles caused by any factor such as the formation of the passivation layer affected the calculated initial olivine dissolution rates. This will be discussed in detail in the following.

4.1.1. Olivine initial dissolution rate as a function of stirring speed

In this study, the initial reaction rate was of interest. Here the initial stoichiometric dissolution rate as a function of angular velocity ω is plotted in Fig. 2 and summarized in Table 2. With the increase of the angular velocity, the dissolution rate decreased first, and then increased before reaching a plateau. The initial unusual decreasing trend was because Fe_2O_3 was formed on the olivine particle surface along with olivine dissolution during the reaction, which will be discussed in the following sub-sections.

Because Fe_2O_3 was formed on the olivine particle surface to hinder dissolution to some extent by reducing the reactive olivine particle surface, Fe_2O_3 was treated as a passivation layer. Therefore, the olivine dissolution rate obtained here was a net rate which was the result of the competition between olivine dissolution and Fe_2O_3 passivation layer formation.

4.1.2. Fluid chemistry analysis and interpretation

As shown in Fig. 3(a), (c), (e), (g) and (i), the concentrations c(Si) of Si and c(Mg) of Mg increased with time in a manner that generally conformed to Eq. (10) with time constants τ that depended upon the stirring rate. However, the apparent equilibrium concentrations obtained in each experiment varied and, in some cases, the time evolution appears to be characterised by more than one time constant. The apparent equilibrium concentrations of Mg: $c_{e,Mg}$, and of Si: $c_{e,Si}$, are summarized in Table 3. The apparent equilibrium concentrations were higher at angular velocities of 42 s^{-1}, 105 s^{-1} and 120 s^{-1}, but were lower at 73 and 89 s^{-1}, which was attributed to the differing competition between the rates of olivine dissolution and Fe_2O_3 formation rates, which will be further discussed in Section 4.1.4. The attainment of near-equilibrium conditions was more evident at 42 s^{-1}, 105 s^{-1} and 120 s^{-1}. The maximum c(Si) and c(Mg) for 73 and 89 s^{-1} were below 0.18 mmol·l^{-1}, which were lower than those in the other cases, indicating slower net olivine dissolution in the case of medium angular velocity. At

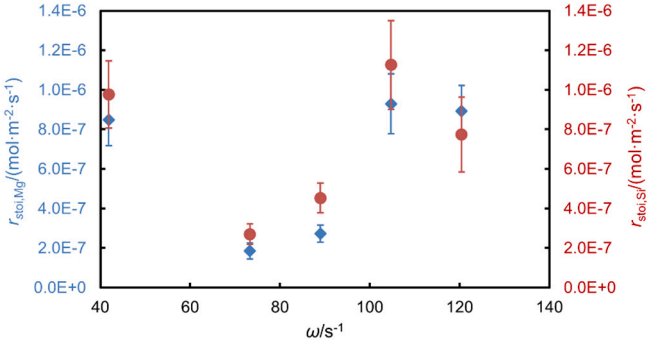


Fig. 2. Olivine initial stoichiometric dissolution rate $r_{stoi,x}$ (x = Mg or Si) with standard uncertainty $u(r_{stoi,x})$ against angular velocity ω. ◆, Mg; ●, Si.

Table 2
Olivine initial stoichiometric dissolution rate $r_{stoi,x}$ (x = Mg or Si) with standard uncertainty $u(r_{stoi,x})$ at different angular velocity ω [a], at temperatures T and CO_2 pressures p_{CO2}.

ω	T	p_{CO2}	$10^7\ r_{stoi,Mg}$	$10^7\ u(r_{stoi,Mg})$	$10^7\ r_{stoi,Si}$	$10^7\ u(r_{stoi,Si})$
s^{-1}	K	MPa	(mol·m^{-2}·s^{-1})		(mol·m^{-2}·s^{-1})	
42	473.0	15.6	8.5	1.3	9.8	1.7
73	472.7	15.6	1.8	0.4	2.7	0.5
89	472.4	15.5	2.7	0.4	4.5	0.8
105	472.6	15.6	9.3	1.5	11.3	2.2
120	472.6	15.5	8.9	1.4	7.7	1.9

[a] The standard uncertainty $u(\omega)$ of ω is 0.6 s^{-1}.

low angular velocity: 42 s^{-1}, the maximum c(Si) and c(Mg) were the highest among all the cases, indicating fast olivine dissolution.

At medium angular velocity: 73 and 89 s^{-1}, c(Si) was either higher than c(Mg) or fairly close to c(Mg), indicating that olivine underwent non-stoichiometric dissolution, while at low angular velocity: 42 s^{-1}, and high angular velocity: 105 and 120 s^{-1}, the c(Si) was lower than c(Mg), suggesting much more stoichiometric olivine dissolution in these cases. This can also be seen in Fig. 3(b), (d), (f), (h) and (j), which plot c(Mg)/c(Si). While c(Mg)/c(Si) was below 1 and 1.3 for 73 and 89 s^{-1}, respectively, for 42, 105 and 120 s^{-1}, c(Mg)/c(Si) was close to 1.8, which was the ratio between Mg and Si in the chemical formula of olivine used in this study.

The concentration profiles for Fe as a function of reaction time are shown in Fig. 4. The concentrations c(Fe) of Fe from the 1st sample in all cases were between 0.019 and 0.064 mmol·l^{-1}, which were either lower than or close to the c(Fe) from the 1st sample (0.05 mmol·l^{-1}) in the blank test discussed in Supplementary information (SI D), indicating that the measured c(Fe) values may not be reliable due to contamination from the measurement system. Thus, to validate the measured c(Fe), an additional sample was collected directly from reactor 2 using a pipettor at the conclusion of the experiment, after reactor 2 was opened.

The concentrations of Fe of this additional sample c_{add}(Fe) (where measured) and the last sample collected during the reaction c_{last}(Fe) were summarized in Table 4. The c(Fe) of both samples should have been close if no Fe had been produced by the sampling system because both samples experienced nearly the same reaction time. However, as shown in Table 4, c_{last}(Fe) was higher than c_{add}(Fe) by 4.4 to 10 times, indicating that there was a much higher amount of Fe produced by the sampling system compared with the Fe released from olivine. Therefore, it was concluded that the measured values of c(Fe) were not reliable due to the contamination from the system.

Nevertheless, useful information was obtained from the trend of c(Fe) as a function of reaction time. As shown in Fig. 4, c(Fe) decreased with increasing the reaction time. The decreasing trends of c(Fe) indicated the consumption of Fe in the aqueous phase. Photos of the unreacted and reacted olivine particles are shown in Fig. 5. The initially green olivine particle turned brown after reaction, indicating the oxidation of Fe^{2+} along with olivine dissolution. Although the whole system including the water had been degassed before starting the experiment, either O_2 might not have been fully removed or it might be present as a trace impurity in the CO_2. It was interesting to note that the colour of the reacted olivine particles was darker at ω = 42, 105 and 120 s^{-1}, where olivine dissolved faster and to a greater extent, while that of reacted olivine particles were lighter at ω = 73 and 89 s^{-1}, where olivine was dissolved slower and to a lesser extent. The intensity of the brown colour suggested the amount of the oxidized iron-rich layer presented on the surface of olivine particles.

4.1.3. Mineralogical analysis and interpretation

To further confirm the chemical state of Fe in the reacted olivine particles, XPS analysis was conducted. It is important to note that due to the rough and irregular shape of the olivine particles, an uneven surface

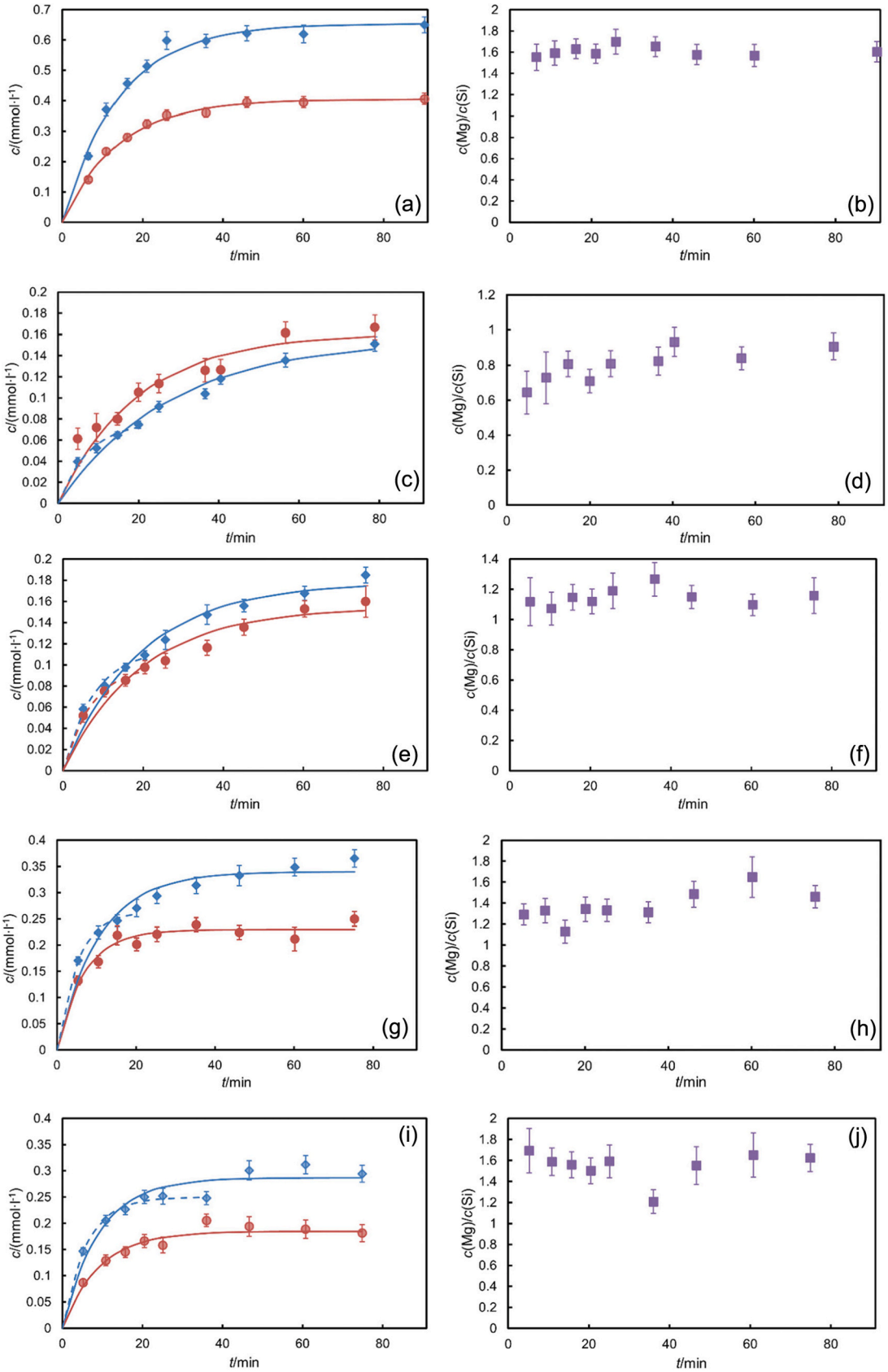


Fig. 3. Concentration c profiles of Mg and Si as a function of reaction time t at (a) $\omega = 42\ s^{-1}$, (c) $\omega = 73\ s^{-1}$, (e) $\omega = 89\ s^{-1}$, (g) $\omega = 105\ s^{-1}$ and (i) $\omega = 120\ s^{-1}$. ◆, Mg; ●, Si; —, fitting curves for all data; - - -, fitting curves for initial periods to better represent the initial dissolution rate when overall fitting did not capture it accurately. Concentration ratio profiles between c(Mg) and c(Si) as a function of reaction time t at (b) $\omega = 42\ s^{-1}$, (d) $\omega = 73\ s^{-1}$, (f) $\omega = 89\ s^{-1}$, (h) $\omega = 105\ s^{-1}$ and (j) $\omega = 120\ s^{-1}$.

Table 3
Apparent equilibrium concentrations $c_{e,Mg}$ for Mg and $c_{e,Si}$ for Si, and liquid volume used in the batch reaction experiment for experiments conducted at different angular velocity ω.

ω/s^{-1}	$c_{e,Mg}$/(mmol·l^{-1})	$c_{e,Si}$/(mmol·l^{-1})	V/ml
42	0.65	0.41	275
73	0.16	0.16	275
89	0.18	0.15	275
105	0.34	0.23	275
120	0.29	0.18	315

with different height was generated when mounting the olivine particles on the sample plate. Thus, when the olivine particles were irritated by X-rays up to 10 nm from the sample surface, some regions revealed more bulk material, while others reflected more surface composition. This led to variability in bulk and surface contributions in the analysis. Furthermore, less than 1 mg of reacted olivine particles were used for XPS analysis, while about 1 g of olivine particles were used in each experiment. Nevertheless, the XPS analysis results provided valuable insights into the qualitative and quantitative surface composition of the reacted olivine particles.

The XPS spectra Fe 2p and O 1s of unreacted olivine, Fe_2O_3, FeO(OH) (Goethite), reacted olivine particles for experiments conducted at $\omega = 42\ s^{-1}$, $\omega = 73\ s^{-1}$, $\omega = 89\ s^{-1}$, $\omega = 105\ s^{-1}$ and $\omega = 120\ s^{-1}$ are shown in Fig. E.1 (Supplementary information SI E). The XPS spectra of Fe 2p, Si 2p, Mg 2p and O1s normalized to the area of the fitted peak Si $2p_{3/2}$ of olivine for unreacted and reacted olivine particles are shown in Fig. E.2 (Supplementary information SI E). The atomic ratios for unreacted and reacted olivine particles based on XPS analysis are summarized in Table E.1 (Supplementary information SI E). The peak fitting of XPS spectra is given in Supplementary information SI B.

The quantification of the amount of Fe_2O_3 presented on the surface of olivine particles was achieved by peak fitting the spectra O 1s, given that the binding energies of O 1s are (531.09 ± 0.30) eV for olivine, and (529.64 ± 0.72) eV for Fe_2O_3. The composition quantification of the top

Table 4
The concentrations of Fe of additional sample c_{add}(Fe) and the last sample collected during the reaction c_{last}(Fe).

ω/s^{-1}	c_{last}(Fe)/ (mmol·l^{-1})	$u[c_{last}(Fe)]$/ (mmol·l^{-1})	c_{add}(Fe)/ (mmol·l^{-1})	$u[c_{add}(Fe)]$/ (mmol·l^{-1})
42	0.0063	0.0003		
73	0.0033	0.0014		
89	0.0031	0.0001	0.0003	0.0001
105	0.0022	0.0001	0.0005	0.0002
120	0.0050	0.0007	0.0006	0.0004

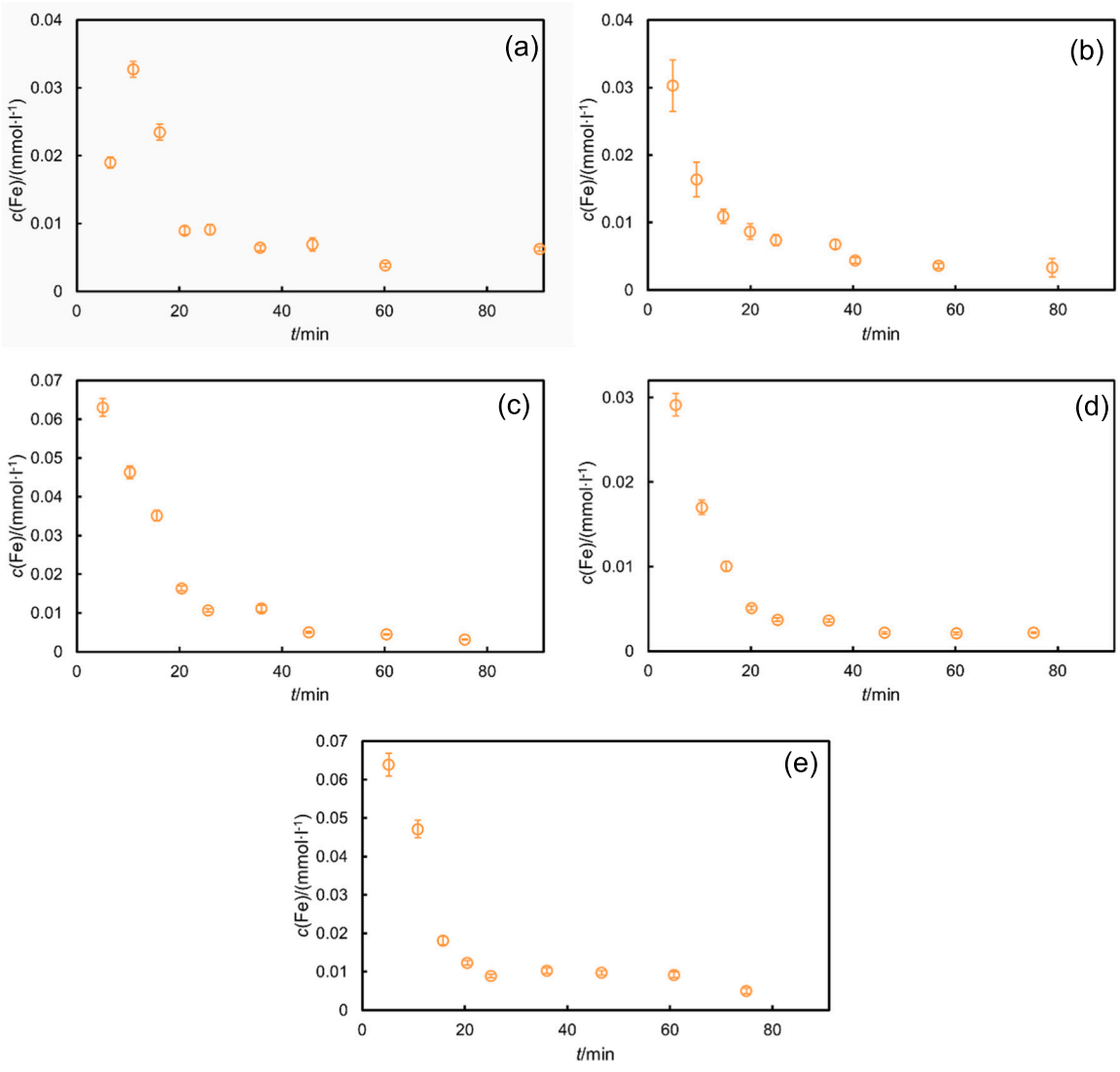


Fig. 4. Concentration c profiles of Fe as a function of reaction time t at (a) $\omega = 42\ s^{-1}$, (b) $\omega = 73\ s^{-1}$, (c) $\omega = 89\ s^{-1}$, (d) $\omega = 105\ s^{-1}$ and (e) $\omega = 120\ s^{-1}$.



Fig. 5. Photos of the unreacted olivine particles, and reacted olivine particles at $T = 473$ K, and $p_{CO2} = 15.6$ MPa. From left to right: $\omega = 120$ s^{-1}, $\omega = 105$ s^{-1}, $\omega = 89$ s^{-1}, $\omega = 73$ s^{-1}, $\omega = 42$ s^{-1} and unreacted olivine particles.

Table 5
The comparison between the amount of dissolved olivine m_{diss}, the molar percentages x_{Fe2O3} of Fe_2O_3, and the intensity of the brown colour of the reacted olivine particles.

ω/s^{-1}	m_{diss}/g	$u(m_{diss})$/g	x_{Fe2O3} [a]	Photos of reacted olivine particles	Colour
42	0.0155	0.0006	26 [b]		Dark brown
73	0.0051	0.0003	28		Light brown
89	0.0053	0.0003	15		Light brown
105	0.0092	0.0004	58		Dark brown
120	0.0080	0.0002	47		Dark brown

[a] The standard relative uncertainty of x_{Fe2O3} is $u_r(x_{Fe2O3}) \leq 7$ %.
[b] The low x_{Fe2O3} at 42 s^{-1} was likely because the XPS analysis mainly captured the bulk material instead of the surface composition of this sample.

10 nm of the reacted olivine particle surface is summarized in Table 5. The molar percentages of Fe_2O_3 x_{Fe2O3} present on the reacted olivine particle surface were higher at stirring rates of 105 and 120 s^{-1} (58 % and 47 %) than at the lower rates of 73 and 89 s^{-1} (28 % and 15 %), as also indicated by the intensity of the brown colour of the reacted olivine particle shown in Fig. 5, and the shapes of the Fe 2p satellite peaks for Fe^{3+} shown in Fig. E.1. However, a low molar percentage of Fe_2O_3 at 26 % was observed at 42 s^{-1}, which did not match the darker brown colour, but agreed with the less distinct Fe 2p satellite peaks observed at 42 s^{-1} shown in Fig. E.1. Therefore, it was confirmed again that the XPS analysis results of this sample mainly revealed the bulk material instead of the surface composition.

Although SiO_2 was formed, its molar percentage was much lower (<4 %) than that of Fe_2O_3 in all cases, so SiO_2 was not discussed in detail here.

4.1.4. *Reaction mechanisms of Fe_2O_3 formation*

Here, three possible hypotheses of the oxidation of Fe^{2+} are discussed in the light of the experimental evidence.

Hypothesis 1. Fe^{2+} was oxidized in-situ on the olivine particle, as illustrated by Eq. (11), which is a general reaction for serpentinization of olivine [35,36].

$$\left(Mg_{1.8},Fe_{0.2}\right)SiO_4(s)+H_2O(aq)\rightarrow\left(Mg_xFe^{II}_yFe^{III}_{3-x-y}\right)\left(Si_zFe^{III}_{2-z}\right)O_5(OH)_4(s)\pm\left(Mg_wFe^{II}_{1-w}\right)(OH)_2(s)\pm Fe^{II}Fe^{III}_2O_4(s)+H_2(g) \quad (11)$$

The serpentinization of olivine has been observed in various geological environments with diverse fluid and rock compositions, and at a wide temperature range: above 673.15 K in subduction zones or the mantle wedge, and below 673.15 K in abyssal peridotites near mid-ocean ridges [37–39]. In this reaction the ferrous iron from olivine is oxidized to ferric iron, which is present in both serpentine (the first product) and magnetite (the third product), whereas H_2O is reduced to H_2 [36]. The serpentinization of olivine has been studied in a wide temperature (413.15 to 673.15 K) and pressure (1 to 300 MPa) range and in different solution [35,40–53]. The serpentinization rates reported in these studies increased first, passed a maximum at temperatures between 523 and 573 K, and finally decreased, with the increase of temperature. These serpentinization rates were generally between (10^{-11} and 10^{-6}) mol·m^{-2}·s^{-1}, except for those reported by Andreani et al. [40], which were notably higher: between (10^{-4} and 10^{-5}) mol·m^{-2}·s^{-1}.

At temperatures between 423 and 473 K, the serpentinization rates ranged from (10^{-10} to 10^{-7}) mol·m^{-2}·s^{-1}, which were lower than the olivine dissolution rates at the same temperature range as determined in

this study (10^{-7} to 10^{-5} mol·m^{-2}·s^{-1}, which will be discussed in Section 4.2.4). In the presence of both serpentinization and olivine dissolution, these processes likely compete. Serpentinization at lower temperatures has also been investigated in the literature. Neubeck et al. [54] studied the serpentinization of olivine at temperatures between 303.15 and 343.15 K, with H_2 detected in their work. Ellison et al. [55] investigated the mineralogy of the cores from the Samail ophiolite in Oman, and the corresponding aqueous geochemistry, and found that the continued alteration of fully serpentinized rocks at low temperatures (below 323 K) can be associated with the production of H_2 in this formation.

Hypothesis 2. Fe^{2+} was first released to the liquid, oxidized in solution, and finally Fe_2O_3 re-precipitated on the olivine particle surface, as illustrated by Eqs. (12)–(15). Fe^{2+} was released from olivine via its dissolution in CO_2-saturated water. The reaction between CO_2 and water is illustrated by Eqs. (1)–(2). The dissolution of olivine is represented by

$$\left(Mg_{1.8},Fe_{0.2}\right)SiO_4(s)+4H^+(aq)=1.8Mg^{2+}(aq)+0.2Fe^{2+}(aq)+H_4SiO_4(aq). \quad (12)$$

Another pathway of Fe^{2+} generation was its release from the Hastelloy reactors and other Hastelloy wetted parts through their reaction with CO_2-acidified water. According to Supplementary information SI D, the CO_2-saturated water that was transferred to reactor 2 already contained the released Fe^{2+} from reactor 1 and its associated wetted parts. However, as discussed in Supplementary information SI D, the average of Fe concentration in the blank test (excluding the 1st sample) was only 0.007 mmol·l^{-1}. This minimal amount of Fe^{2+} released from the reactor system was unlikely to independently induce Fe_2O_3 formation, as no Fe_2O_3 was visibly observed in the blank test.

In this hypothesis, some Fe^{2+} was oxidized, resulting in the formation of Fe_2O_3, as represented by Eqs. (13)–(15). The oxidation of ferrous iron in the solution and the formation of $Fe(OH)_3$ is illustrated by [56].

$$Fe^{2+}(aq)+\frac{1}{4}O_2(aq)+\frac{5}{2}H_2O(aq)=Fe(OH)_3(s)+2H^+(aq). \quad (13)$$

Fe_2O_3 is usually formed via a two-step transformation [57–61]. $Fe(OH)_3$ would typically transform to FeO(OH) first, which is represented by [57–61]

$$Fe(OH)_3(s)=FeOOH(s)+H_2O(aq). \quad (14)$$

Fe_2O_3 could then be formed through the dehydration and/or dihydroxylation of FeO(OH) and is represented by [57–61].

$$2FeOOH(s)=Fe_2O_3(s)+H_2O(aq). \quad (15)$$

FeO(OH) is generally considered an intermediate in the transformation [57–61]. Because no FeO(OH) was detected based on the XPS analysis, its presence was likely too short-lived to be captured.

Hypothesis 3. The third possibility is that both of these processes occurred in parallel. Because in-situ analysis during the reaction was not available, it was difficult to validate the first hypothesis, while the decreasing trends of c(Fe) in Fig. 4 indicated the consumption of Fe in the aqueous phase, which supported the second hypothesis. The decreasing trend of c(Fe) was only observed when the reacted olivine particles turned brown after reaction, while a totally different trend was observed in the other cases which will be discussed in the next section. Therefore, the second hypothesis is more likely to be correct.

Until now, it was clear that the precipitated Fe_2O_3 covered some of the surface of the olivine particles, so the reactive surface area of the olivine particles was reduced. The amount of precipitated Fe_2O_3 was proportional to the amount of olivine that dissolved, because more released Fe^{2+} was available to be oxidized if more olivine was dissolved. The brown colour of the reacted olivine particles was darker when a higher amount of Fe_2O_3 was presented. In short, more olivine dissolved caused more Fe_2O_3 formed on the surface of the remaining olivine particles, which caused a darker brown colour. This is shown in Table 5, which summarizes and compares the qualitative intensity of the brown colour, the percentages of Fe_2O_3, and the amount of dissolved olivine m_{diss} which is given by

$$m_{diss}=0.5\{c_{last}(Mg)VM_{olivine}/1.8+c_{last}(Si)VM_{olivine}\}, \quad (16)$$

where c_{last}(Mg) and Si c_{last}(Si) are the concentrations of Mg and Si from the last sample, respectively, V is the liquid volume, and $M_{olivine}$ is the molar mass of olivine, which was 147 g·mol^{-1}.

As shown in Table 5, only about 0.005 g of olivine was dissolved at 73 and 89 s^{-1}, resulting in low molar percentages of Fe_2O_3 at 28 % and 15 % and a lighter brown colour of the reacted particles. In contrast, more than 0.008 g of olivine was dissolved at 105 and 120 s^{-1}, leading to higher molar percentages of Fe_2O_3 at 58 % and 47 %, and a darker brown colour. The experiment performed at 42 s^{-1} did not follow the same trend as the experiments conducted at 105 and 120 s^{-1} because more bulk material was captured by the XPS analysis, which has been discussed. Because m_{diss} was calculated based on c_{last}(Mg) and c_{last}(Si), higher concentrations of Mg and Si were measured when a darker brown colour of reacted olivine particles was observed. Besides, a higher concentration of Fe in the aqueous phase after the completion of the reaction was also observed when there was a higher m_{diss}, even with the precipitated Fe_2O_3. As shown in Table 4, c_{add}(Fe) was 0.0005 and 0.0006 mmol·l^{-1} at 105 and 120 s^{-1}, which were higher than 0.0003 mmol·l^{-1} at 89 s^{-1}.

Although the precipitated Fe_2O_3 reduced the reactive surface of olivine particles, the darker colour or higher amount of Fe_2O_3 did not mean less olivine was dissolved, because compared with the olivine particles ranging between (106 and 212) μm used in this study, the Fe_2O_3 precipitates were only at the nanometer scale. Therefore, the precipitated Fe_2O_3 did not completely hinder the dissolution of olivine. It is essential to note that the recovered reacted olivine particles can only reveal the end status of the reaction, but not the initial reaction rate or initial stage. The SEM images with EDX analysis of unreacted olivine particles and the recovered reacted olivine particles from the experiments performed at ω = (42, 73 and 105) s^{-1} are shown in Figs. E.3 and E.4.

The two possible mechanisms of Fe_2O_3 formation (in-situ and ex-situ oxidation of Fe^{2+}) are illustrated in Fig. 6, where the olivine particle surface, the static boundary layer with respect to the olivine particle surface, the bulk solution and the gas phase are shown. The liquid flow velocity was high in the bulk solution, whereas it decreased in the boundary layer. The substance transport in the boundary layer was through diffusion driven by concentration difference. With the increase of angular velocity, the thickness of the boundary layer decreased and became negligible, and consequently the diffusion process became quicker (because of the thinner boundary layer) and nearly disappeared when the boundary layer was negligible. At low angular velocity (42 s^{-1}) at which the olivine particles remained stationary at the bottom of reactor 2, the boundary layer was thick, so diffusion was necessary for substance transport between the bulk solution and the olivine particle surface. To initiate olivine dissolution, H^+ diffused from the bulk solution to the olivine particle surface, crossing the boundary layer. As a result, Mg^{2+}, Fe^{2+} and H_4SiO_4 were produced (Eq. (12)). These steps were illustrated by steps (1)–(3) in Fig. 6.

For surface crystallization (heterogeneous nucleation) of Fe_2O_3, O_2 diffused from the bulk solution to the olivine particle surface, where Fe^{2+} was oxidized, after which the solution became supersaturated with respect to $Fe(OH)_3$, so $Fe(OH)_3$ nuclei were formed on the olivine particle surface (Eq. (13)). The other source of Fe^{2+} was the Hastelloy reactors and Hastelloy wetted parts, which released Fe^{2+} via their reaction with CO_2-acidified water. As mentioned earlier, the CO_2-saturated water that was transferred to reactor 2 already contained the released Fe^{2+} from reactor 1 and its associated wetted parts, so the Fe^{2+} from reactor 1 pre-existed in the solution. The $Fe(OH)_3$ nuclei then continued to grow

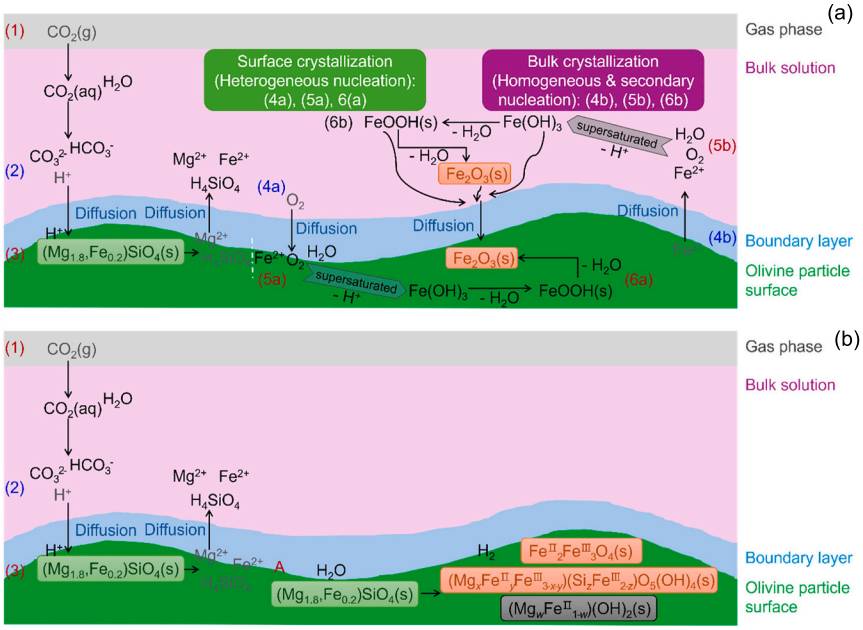


Fig. 6. Schematic diagrams of Fe_2O_3 formation on the surface of olivine particles. (a) Olivine dissolution in CO_2-saturated water, realising Fe^{2+}, Mg^{2+} and H_4SiO_4 (steps (1)–(3)), followed by Fe_2O_3 precipitation via surface crystallization (steps (4a)–(6a)) and/or bulk crystallization (steps (4b)–(6b)); (b) in-situ oxidation of Fe^{2+} via serpentinization of olivine (step A) alongside olivine dissolution in CO_2-saturated water (steps (1)–(3)). The red numbering denotes reactions, the blue numbering denotes diffusion, and the black numbering denotes reactions coupled with transport, excluding diffusion.

via further precipitation, subsequently forming $Fe(OH)_3$ crystal and coating layers, followed by the stepwise transformation of $Fe(OH)_3$, consequently leading to the formation of Fe_2O_3 on the olivine particle surface (Eq. (15)), as illustrated by steps (4a)–(6a) in Fig. 6(a). It is worth mentioning that, compared with H^+, the concentration of O_2 in the bulk solution was significantly lower. Additionally, the diffusion coefficient of O_2 is generally lower than that of H^+ in water under the same condition [62–66]. Therefore, according to Fick's first law, the diffusion of O_2 from the bulk solution to the olivine particle surface was much slower than that of H^+.

For bulk crystallization (homogeneous and secondary nucleation) of Fe_2O_3, the Fe^{2+} released from olivine particles diffused to the bulk solution, where Fe^{2+} was oxidized, after which the solution became supersaturated with respect to $Fe(OH)_3$, so $Fe(OH)_3$ was formed (Eq. (13)). The Fe^{2+} released from the Hastelloy reactors and wetted parts might also be involved in the reaction. Subsequently, the $Fe(OH)_3$ nuclei and/or their crystalline form, and/or the first transformation product: FeO(OH) precipitates, and/or the final transformation product: Fe_2O_3 precipitates, transported from the bulk solution to the boundary layer, followed by the diffusion of one or more of these substances from the boundary layer to the olivine particle surface. For the transport of Fe$(OH)_3$ nuclei and/or their solid crystal form, and/or FeO(OH) precipitates, and/or Fe_2O_3 precipitates from the bulk solution to the boundary layer, and the eventual formation of Fe_2O_3 passivation layer on the olivine particle surface, the following inferences were made. The diffusion step from the boundary layer to the olivine particle surface was clear, so it was not mentioned in the following inference.

$Fe(OH)_3$ nuclei have high surface energy [67–70], making them unstable in solution and prone to attaching to the olivine particle surface, the imperfections on which such as defects and cracks likely acted as nucleation sites, to reduce the free energy of the nuclei and stabilize them. Subsequently they were promoted to grow into $Fe(OH)_3$ coatings via further $Fe(OH)_3$ precipitation. Fe_2O_3 layer was then formed via the stepwise transformation of $Fe(OH)_3$. At high angular velocity, the strong advection induced by stirring enhanced the movement of $Fe(OH)_3$ nuclei towards the olivine particle surface, whereas at low angular velocity, Brownian motion played an important role in its transport from the bulk solution to the boundary layer.

In the case of $Fe(OH)_3$, and/or FeO(OH) and/or Fe_2O_3 precipitates, larger particles gradually deposited onto the olivine surface due to gravity, at low angular velocity and especially when the olivine particles stayed stationary at the bottom of reactor 2, whereas for small particles such as nanoscale particles, Brownian motion likely became important for their transport from the bulk solution to the boundary layer. At high angular velocity where the contents were well stirred, the transport of Fe$(OH)_3$, and/or FeO(OH) and/or Fe_2O_3 precipitates from bulk solution to the boundary layer was dominated by advection. Frequent collisions between these precipitates and olivine particles enhanced their attachment onto olivine particles. Once they reached the olivine particle surface, some partially dissolved areas might act as adsorption site for Fe$(OH)_3$, and/or FeO(OH) and/or Fe_2O_3 precipitates. Van der Waals forces could also contribute to their adhesion. There might also be chemical bonding between these precipitates and the functional group on the olivine particle surface to stabilize the attachment. Once attached, secondary nucleation could occur at these initial deposit sites, leading to thicker and/or larger Fe_2O_3 layers over time.

Heterogeneous nucleation is more favourable because the energy barrier for initiating crystal growth at an existing solid-liquid interface is lower than that required for homogeneous nucleation, which necessitates forming a new solid-liquid interface in the bulk solution [71–73]. Besides, surface imperfections such as cracks and defects often act as nucleation sites [72,73]. However, although homogeneous nucleation requires more energy, it cannot be entirely excluded here.

In the presence of the boundary layer, i.e. when the angular velocity was not high enough, the formation of Fe_2O_3 required at least one additional diffusion step crossing the boundary layer, compared with olivine dissolution, so the formation of Fe_2O_3 was slower than olivine dissolution. Based on the trend of olivine dissolution rate as a function of angular velocity (shown in Fig. 2), the following inferences were made. At low angular velocity (42 s^{-1}), the following occurred. The individual reaction rates of both Fe_2O_3 formation and olivine dissolution were decreased by the mass transfer effect (substance transport via diffusion in the boundary layer), but Fe_2O_3 was formed much slower than olivine dissolved, so only a tiny portion of the olivine surface was covered with

minimal hindrance to olivine dissolution, hence leading to a high measured net olivine dissolution rate. As a result, the apparent equilibrium concentrations $c_{e,Mg}$ and $c_{e,Si}$ summarized in Table 3 were the highest in this case because of the less effective Fe_2O_3 coating on the olivine particle surface, which allowed more sustained dissolution.

At medium angular velocities (73 and 89 s^{-1}), the individual reaction rates of both reactions increased because of the thinner boundary layer. However, because the Fe_2O_3 formed quicker to cover the reactive olivine surface more effectively than at low angular velocity, the measured net olivine dissolution rates were low. As a result, the apparent equilibrium concentrations $c_{e,Mg}$ and $c_{e,Si}$ summarized in Table 3 were the lowest for medium angular velocities because of the more effective inhibition caused by the formation of Fe_2O_3. At high angular velocities (105 and 120 s^{-1}), the measured net olivine dissolution rate reached a plateau and the mass transfer effect was fully eliminated for both reactions. In this case, the reaction rates of both olivine dissolution and Fe_2O_3 precipitation were increased as the boundary layer was negligible. Although Fe_2O_3 formed much quicker to cover more reactive olivine particle surface (compared to low and medium angular velocities), meanwhile olivine also dissolved much more rapidly (compared to low and medium angular velocities), leading to a high net olivine dissolution rate. As a result, the apparent equilibrium concentrations $c_{e,Mg}$ and $c_{e,Si}$ summarized in Table 3 were at intermediate levels at high angular velocities. The $c_{e,Mg}$ and $c_{e,Si}$ at high angular velocities were lower than those at low angular velocity, which was because Fe_2O_3 more effectively coated the reactive surface of olivine at higher angular velocities, thereby limiting further dissolution.

For the in-situ oxidation of Fe^{2+} via serpentinization of olivine, as shown in Fig. 6(b) and illustrated by Eq. (11), only olivine and water were required for the reaction, so the boundary layer and mass transfer effect had a minimal or even negligible effect on the formation of Fe_2O_3 through this mechanism. Unfortunately, it was not possible to analyze the gas phase during these experiments to determine whether hydrogen was produced.

It is important to note that the analysis of the initial net olivine dissolution rate was not able to explain the amount of Fe_2O_3 formed on the surface of the olivine particles, nor the intensity of the brown colour of the reacted olivine particles. This was because the dissolution rate presented here only reflected the reaction process during a certain initial period, whereas the recovered reacted particles reflected the entirety of the reaction process.

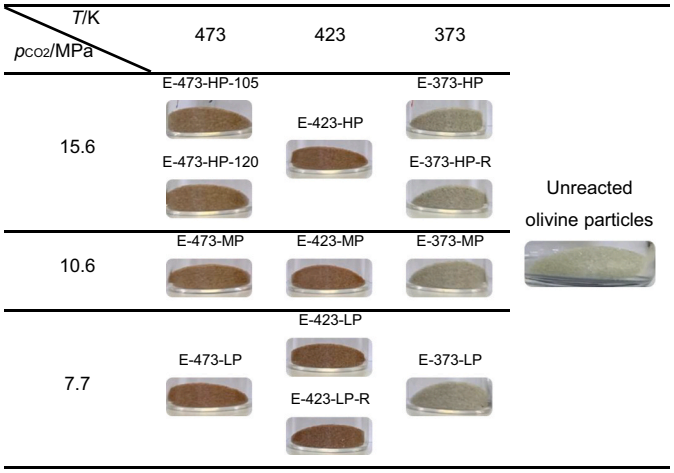
The validation of the observed trend of olivine dissolution rate as a function of angular velocity, based on a series of measurements conducted at different angular velocities, is given in Supplementary information SI F.

Table 6
Experimental conditions for olivine dissolution in CO_2-saturated water at temperature T, pressure p_{CO2} and angular velocity ω [a], in a period t_{total}.

Experiment	t_{total}/min	T/K	p_{CO2}/MPa	ω/s^{-1}
E-473-HP-105	75.3	472.6	15.6	105
E-473-HP-120	74.9	472.6	15.5	120
E-473-MP	75.6	472.8	10.5	110
E-473-LP	75.3	472.9	7.7	110
E-423-HP	74.1	422.8	15.6	110
E-423-MP [b]	54.2	423.1	10.6	110 [b]
E-423-LP	74.7	422.9	7.7	110
E-423-LP-R	75.3	422.8	7.7	110
E-373-HP	75.2	373.0	15.6	110
E-373-HP-R [c]	82.7	373.0	15.6	110 [c]
E-373-MP	75.2	373.0	10.8	110
E-373-LP	75.2	373.1	7.7	110

[a] The standard uncertainty $u(\omega)$ of ω is 0.6 s^{-1}.
[b] Constant angular velocity of 110 s^{-1} was maintained for the first 38 min, after which it fluctuated around a value of about 50 s^{-1}.
[c] There were about 8 min during which there was either no stirring or the angular velocity fluctuated.

Table 7
Photos of the recovered reacted olivine particles at different temperature T and pressure p_{CO2}.



4.1.5. Summary

The apparent initial olivine dissolution rates decreased first, then increased and finally reached a plateau with the increase of angular velocity. The most likely interpretation of the experimental results was that, although the individual reaction rates of olivine dissolution and Fe_2O_3 passivation both increased with increasing angular velocity, the dominant factor changed. Finally, the angular velocity was determined to be 110 s^{-1} for the rest of the experiments.

The finding on the olivine dissolution rate as a function of angular velocity suggested that under reservoir conditions without stirring, the Fe_2O_3 passivation layer would form slowly, allowing rapid olivine dissolution and hence more Mg^{2+} to be released for mineralization.

4.2. Olivine dissolution kinetics and mechanistic behaviour

After the angular velocity was determined, measurements on olivine dissolution in CO_2-saturated water were conducted at pressures between 7.7 and 15.6 MPa and at temperatures of approximately 373, 423 and 473 K. The different experiments are designated by a code in the form *E-*<T>-<P>-<X> where <T> denotes the temperature in kelvin, <P> denotes high (≈15.6 MPa), medium (≈10.6 MPa) or low (≈7.7 MPa) pressure, and <X> is a suffix indicating either the angular stirring velocity (if different to 110 s^{-1}) or "R" for a repeated run. The experimental conditions are summarized in Table 6. The photos of the reacted and unreacted olivine particles are shown in Table 7.

4.2.1. Mineralogical analysis and interpretation

The XPS spectra Fe 2p, Si 2p and O 1s of unreacted olivine, Fe_2O_3, FeO(OH) (Goethite), SiO_2, reacted olivine particles for experiments E-473-HP-105, E-473-HP-120, E-473-MP, E-473-LP, E-423-HP, E-423-MP, E-423-LP, E-423-LP-R, E-373-HP, E-373-HP-R, E-373-MP and E-373-LP, where available, are shown in Fig. G.1 (Supplementary information SI G). The XPS spectra of Fe 2p, Si 2p, Mg 2p and O 1s normalized to the area of the fitted peak Si $2p_{3/2}$ of olivine for unreacted and reacted olivine particles are shown in Fig. G.2 (Supplementary information SI G). The atomic ratios for unreacted and reacted olivine particles based on XPS analysis are summarized in Table G.1 (Supplementary information SI G). The peak fitting of XPS spectra is given in the Supplementary information SI B.

The XPS analysis showed that SiO_2 and Fe_2O_3 formed on the surface of olivine particles. Fe_2O_3 dominated at 423 and 473 K, while SiO_2 dominated at 373 K. As discussed in Supplementary information SI E, the main component of the iron-oxidation layer formed was Fe_2O_3.

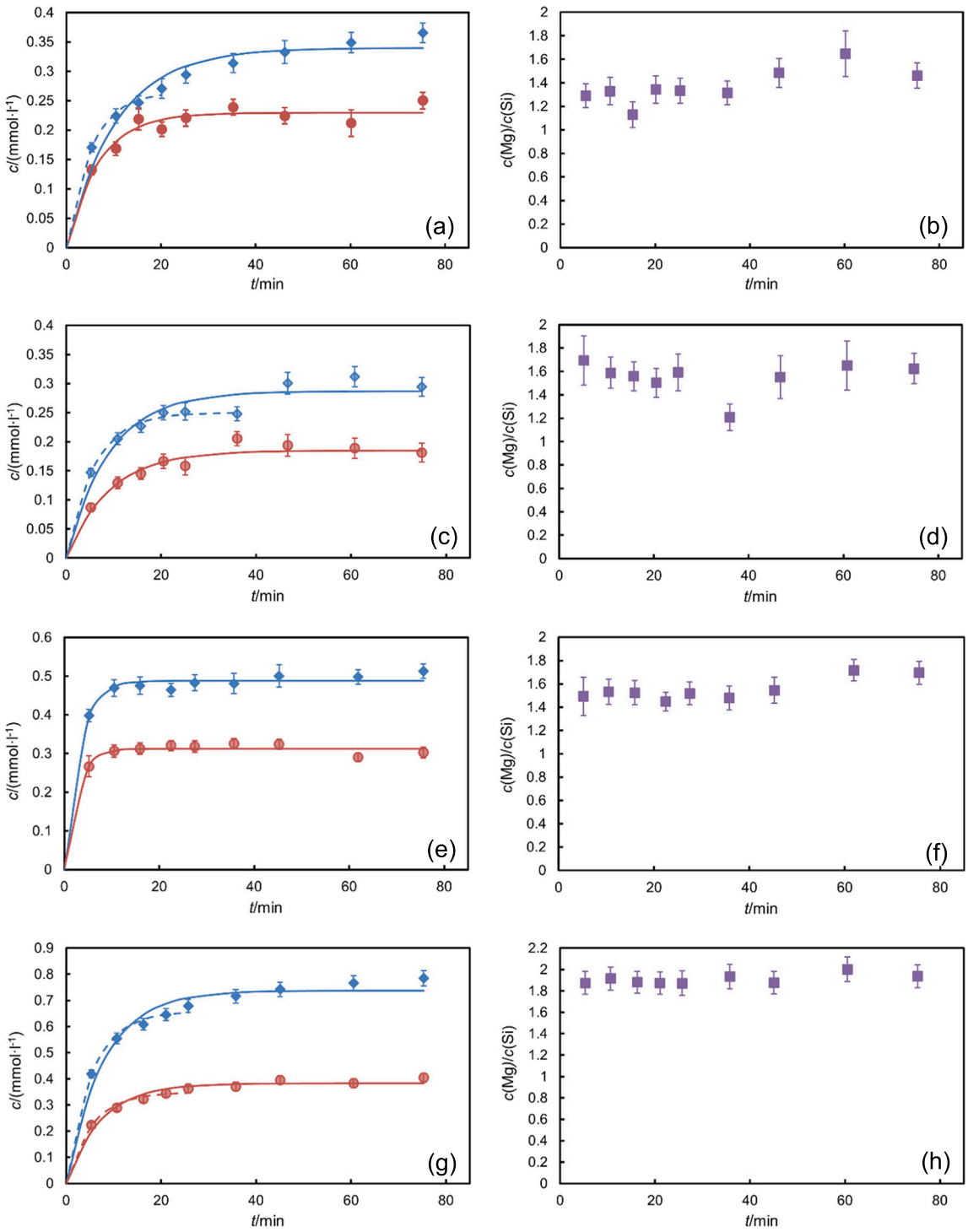


Fig. 7. Concentration c profiles of Mg and Si as a function of reaction time t at 473 K and at (a) $p_{CO2} = 15.6$ MPa and $\omega = 105$ s^{-1} (E-473-HP-105), (c) $p_{CO2} = 15.6$ MPa and $\omega = 120$ s^{-1} (E-473-HP-120), (e) $p_{CO2} = 10.6$ MPa (E-473-MP), and (g) $p_{CO2} = 7.7$ MPa (E-473-LP). $\omega = 110$ s^{-1} for $p_{CO2} = 10.6$ and 7.7 MPa. ◆, Mg; ●, Si; —, fitting curves for all data; - - -, fitting curves for initial periods to better represent the initial dissolution rate when overall fitting did not capture it accurately. Concentration ratio profiles between c(Mg) and c(Si) as a function of reaction time t at 473 K and at (b) $p_{CO2} = 15.6$ MPa and $\omega = 105$ s^{-1} (E-473-HP-105), (d) $p_{CO2} = 15.6$ MPa and $\omega = 120$ s^{-1} (E-473-HP-120), (f) $p_{CO2} = 10.6$ MPa (E-473-MP), and (h) $p_{CO2} = 7.7$ MPa (E-473-LP). $\omega = 110$ s^{-1} for $p_{CO2} = 10.6$ and 7.7 MPa.

Although FeO(OH) was unlikely to be present, possibly because of its near-complete transformation to Fe_2O_3, the presence of a trace amount of FeO(OH) cannot be excluded. For quantification of the surface composition of reacted olivine particles, Fe_2O_3 was assumed to be the only component of the iron-oxidation layer. At higher temperatures, more Fe_2O_3 formed at 423 K than at 473 K. The amounts of Fe_2O_3 formed at 423.15 and 473 K were more than those of SiO_2 formed at 373 K, considering the different amounts of oxygen contributed by SiO_2 and Fe_2O_3.

ToF-SIMS analysis was performed on the recovered reacted olivine particles from experiment E-473-HP-105 and E-423-HP to visualize the distribution of Fe_2O_3, as shown in Supplementary information SI H. Both depth profiling and surface analysis were performed on the recovered reacted olivine particles from experiment E-473-HP-105, whereas only

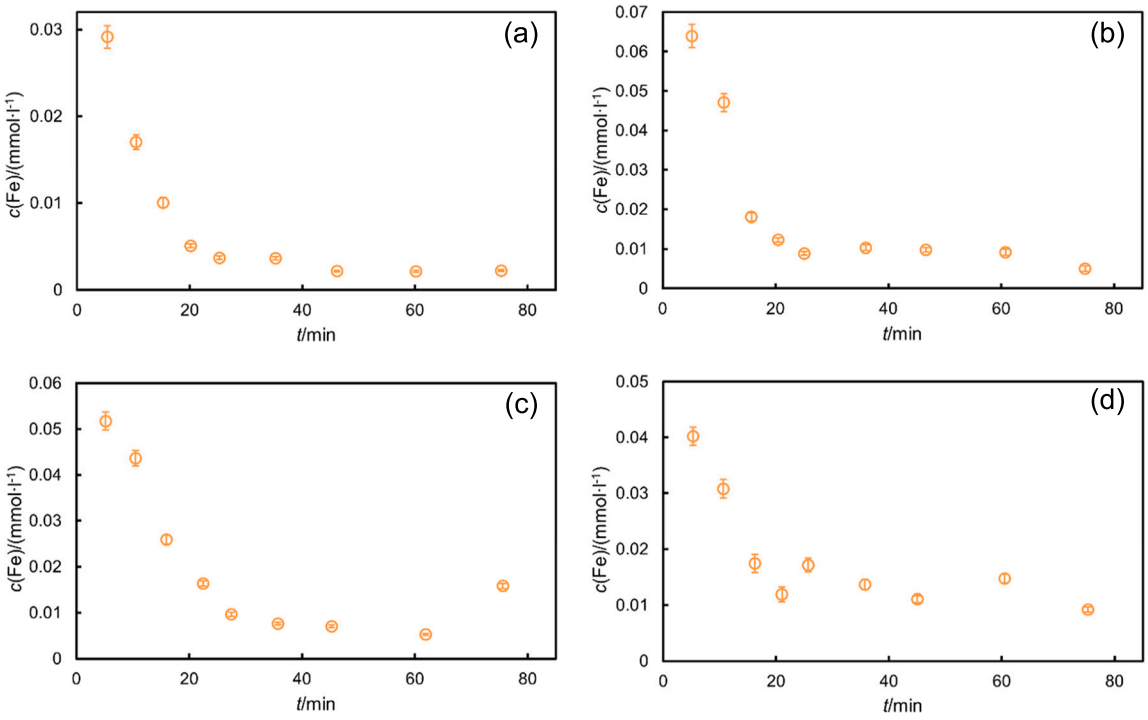


Fig. 8. Concentration c profiles of Fe as a function of reaction time t at 473 K and at (a) $p_{CO2} = 15.6$ MPa and $\omega = 105$ s^{-1} (E-473-HP-105), (b) $p_{CO2} = 15.6$ MPa and $\omega = 120$ s^{-1} (E-473-HP-120), (c) $p_{CO2} = 10.6$ MPa (E-473-MP), and (d) $p_{CO2} = 7.7$ MPa (E-473-LP). $\omega = 110$ s^{-1} for $p_{CO2} = 10.6$ and 7.7 MPa.

surface analysis were performed on the recovered reacted olivine particles from experiment E-423-HP. For depth profiling, because of the formation of Fe_2O_3 on the surface, the Fe^+ signal was more intense on the surface, whereas the Mg^+ and Si^+ signals were stronger in the bulk. For surface analysis, the Fe^+ signal was intense in the area where $Fe_2O_3^+$ was present to cover olivine surface, while the Mg^+ and Si^+ signals were weak in this region.

The SEM images with EDX analysis of unreacted olivine particles and the recovered reacted olivine particles from experiments E-473-HP-120, E-423-LP and E-373-LP are shown in Figs. H.9 and H.10.

4.2.2. Fluid chemistry analysis and interpretation

The concentration profiles of Mg and Si, and the concentration ratio profiles between Mg and Si as a function of reaction time at $p_{CO2} = 15.6$ MPa, and at $T = (473, 423$ and $373)$ K are shown in Figs. 7, 9 and 11, respectively. The concentration c profiles of Fe as a function of reaction time at $T = (473, 423$ and $373)$ K are shown in Figs. 8, 10 and 12, respectively.

As shown in Fig. 7(a), (c), (e) and (g), at 473, c(Mg) and c(Si) increased rapidly in the first 7th to 15th minute, after which the increases slowed down, and c(Mg) and c(Si) approached equilibrium. As shown in Fig. 7(d), (f) and (h), the ratio between c(Mg) and c(Si) was between 1.5 and 1.9, which was close to the ratio between Mg and Si in the chemical formula of olivine used in this study, suggesting near-stoichiometric dissolution, while the ratio between c(Mg) and c(Si) was slightly lower at 1.4 in Fig. 7(b), suggesting the preferential release of Si, which agreed with a higher Mg/Si ratio (1.68) than that of the unreacted olivine particles on the particle surface, as discussed in Supplementary information SI G. However, for E-473-HP-120, although the Mg/Si ratio on the surface was only 1.06 as shown in Table G.1, the ratio profile shown in Fig. 7(d) did not show a distinct preferential release of Mg. This discrepancy may be due to the XPS analysis sample not being fully representative of the overall reaction.

As shown in Fig. 8, at 473 K, c(Fe) decreased during the reaction, indicating the consumption of Fe in the aqueous phase, which agreed with the XPS analysis of the reacted olivine particles that a significant amount of Fe_2O_3 was formed on the particle surface at this temperature. The brown colour of reacted olivine particles observed at 473 K shown in Table 7 also indicated the oxidation of Fe^{2+}.

As shown in Fig. 9(a), (c), (e) and (g), at 423 K, nearly linear increases of c(Mg) and c(Si) as a function of reaction time were observed. To achieve a good fit between the measured concentration data and Eq. (10), the constant c_0 was included. The inclusion of c_0 suggested that olivine dissolution might have been very rapid at the initial stage at 423 K, or c_0 could be attributed to the Mg and Si that were already present in the system before the reaction started. All the cases at this temperature were far from equilibrium. As shown in Fig. 9(b), (d) and (f), the ratio between c(Mg) and c(Si) was between 1.6 and 2.4, which was close to the ratio between Mg and Si in the chemical formula of olivine used in this study, suggesting near stoichiometric dissolution in these experiments, while the ratio between c(Mg) and c(Si) was higher at 2.5 in measurement E-423-LP-R, as shown in Fig. 9(h), which agreed with a low Mg/Si ratio at only 1.22 on the particle surface, shown in Table G.1, so it can be inferred a preferential release of Mg in this case. However, for E-423-HP, although the Mg/Si ratio on the surface was up to 1.88 as shown in Table G.1, the ratio profile shown in Fig. 9(b) did not show a distinct preferential release of Si. This discrepancy may be due to the XPS analysis sample not being fully representative of the overall reaction.

For E-423-MP shown in Figs. 9(c) and (d) and 10(b), the angular velocity was not able to maintain constant at 110 s^{-1} and instead fluctuated around 50 s^{-1} from the 38th minute onwards, which is discussed in Supplementary information SI F.

Measurements E-423-LP-R and E-423-LP were replicate experiments conducted at the same temperature and pressure, but a more rapid dissolution of olivine was observed in measurement E-423-LP than in measurement E-423-LP-R, as shown in Fig. 9(e) and (g). This inconsistent dissolution behaviour was because the stirring system performed differently in measurement E-423-LP-R compared to the other experiments, as discussed in Supplementary information SI I.

Nevertheless, there was no substantial difference in the amount of dissolved olivine or in the concentration profiles of Mg and Si between

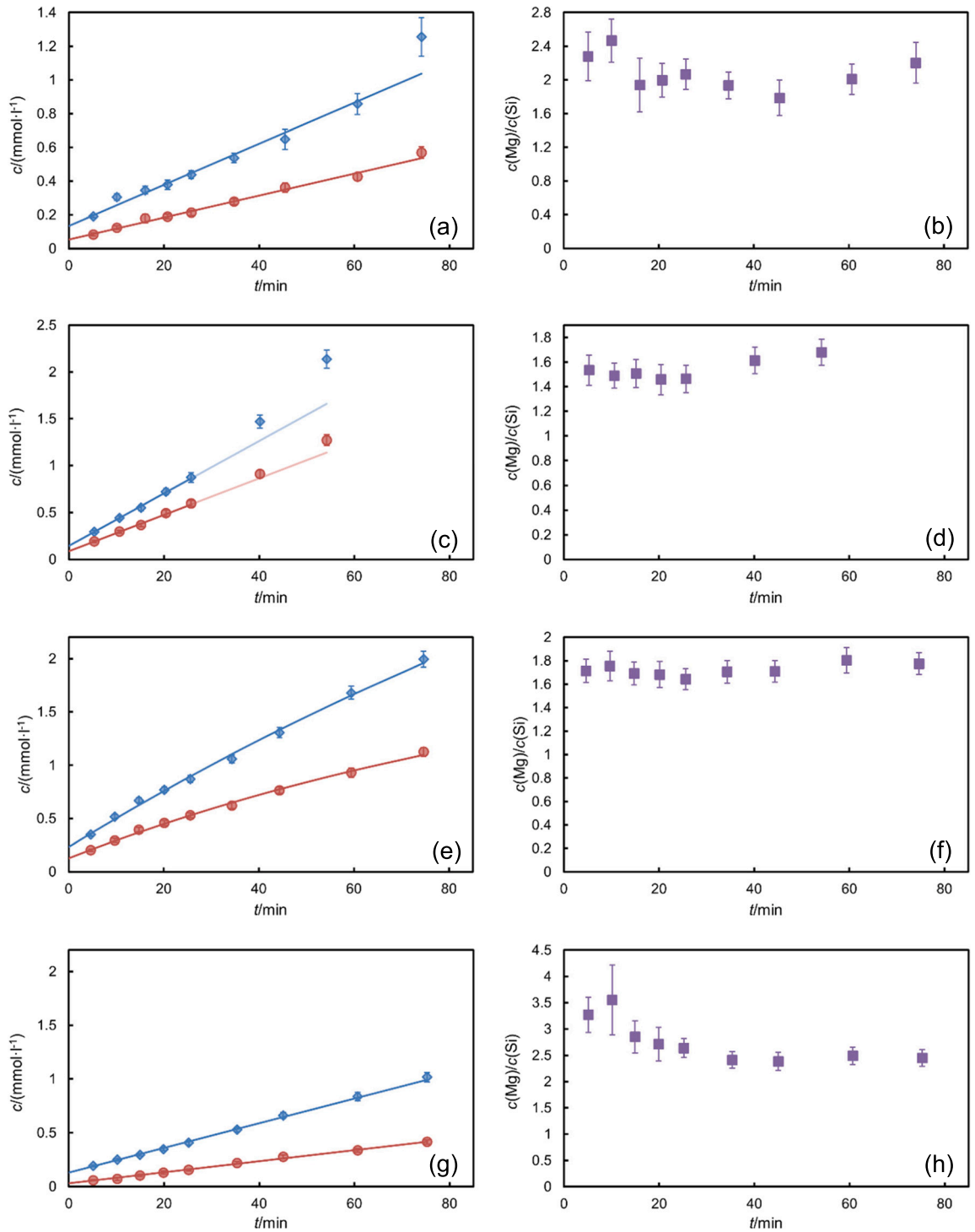


Fig. 9. Concentration c profiles of Mg and Si as a function of reaction time t at 423 K and at (a) $p_{CO2} = 15.6$ MPa (E-423-HP), (c) $p_{CO2} = 10.6$ MPa (E-423-MP), (e) $p_{CO2} = 7.7$ MPa (E-423-LP), and (g) $p_{CO2} = 7.7$ MPa (E-423-LP-R), which is a repeated run with the stirring performed differently from the rest runs. ◆, Mg; ●, Si; —, fitting curves. Concentration ratio profiles between c(Mg) and c(Si) as a function of reaction time t at 423 K and at (b) $p_{CO2} = 15.6$ MPa (E-423-HP), (d) $p_{CO2} = 10.6$ MPa (E-423-MP), (f) $p_{CO2} = 7.7$ MPa (E-423-LP), and (h) $p_{CO2} = 7.7$ MPa (E-423-LP-R), which is a repeated run with the stirring performed differently from the rest runs.

measurements E-423-LP and E-423-LP-R. About twice the amount of olivine was dissolved in measurement E-423-LP compared to measurement E-423-LP-R.

As shown in Fig. 10, at 423 K, c(Fe) decreased during the reaction, indicating the consumption of Fe in the aqueous phase, which agreed with the XPS analysis of the reacted olivine particles that a considerable amount of Fe_2O_3 was formed on the particle surface at 423 K. The brown colour of the reacted olivine particles shown in Table 7 also indicated the Fe^{2+} had been oxidized at this temperature.

As shown in Fig. 11(a), (c), (e) and (g), at 373 K, c(Mg) and c(Si) increased rapidly in the first 20th to 25th minute, after which the increases slowed down, but the near-equilibrium state was only observed in Fig. 11(a) and (g). It took a longer time for measurements E-373-HP and E-373-LP to approach equilibrium than all the runs conducted at

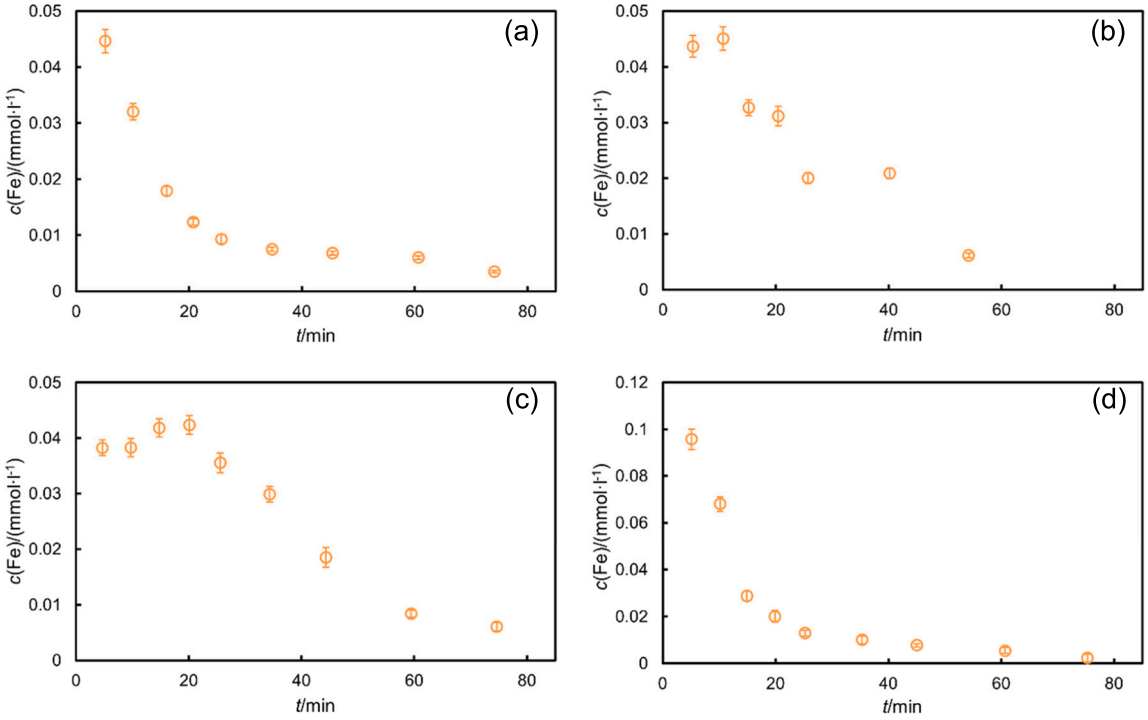


Fig. 10. Concentration c profiles of Fe as a function of reaction time t at 423 K and at (a) $p_{CO2} = 15.6$ MPa (E-423-HP), (b) $p_{CO2} = 10.6$ MPa (E-423-MP), (c) $p_{CO2} = 7.7$ MPa (E-423-LP), and (d) $p_{CO2} = 7.7$ MPa (E-423-LP-R), which is a repeated run with the stirring performed differently from the rest runs.

473 K shown in Fig. 7. As shown in Fig. 11(b), (d), (f) and (h), the ratio between c(Mg) and c(Si) was between 1.7 and 1.9 which was close to the ratio between Mg and Si in the chemical formula of olivine used in this study, suggesting stoichiometric dissolution. The ratio profile for E-373-HP shown in Fig. 11(b) did not show a distinct preferential release of Mg, although the ratio Mg/Si on the particle surface was 1.17, shown in Table G.1, which was likely because the XPS analysis sample not being fully representative of the overall reaction.

According to the XPS analysis earlier, a considerable amount of SiO_2 was formed at 373 K. The released c(Si) to the aqueous phase was not able to prove the formation of silicon-rich layer if this layer only had a thickness between 15 and 40 nm, because such a thin layer only consumed no more than 0.01 % of the released Si [23]. For all cases at 373 K in this work, the XPS analysis detected both SiO_2 and olivine within the top 10 nm of the surface, indicating that the SiO_2 layer was likely less than 10 nm thick. Consequently, no decrease in the c(Si) was observed, as the formation of such a thin SiO_2 layer would not significantly affect the overall Si release.

E-373-HP-R (Figs. 11(c) and (d), and 12(b)) was a repeated experiment with a brief period during which the stirring was not stable, which is discussed in Supplementary information SI F.

As shown in Fig. 12, at 373 K, c(Fe) increased during the reaction, which was different from the decreasing trend of c(Fe) as a function of reaction time t at 473 and 423 K. The increasing trend of c(Fe) suggested the accumulation of Fe released to the aqueous phase, which agreed with the XPS analysis that only little Fe_2O_3 was formed on the surface at 373 K. The colour of the reacted olivine particles was another indicator. As shown in Table 7, the reacted olivine particles was slightly yellowish green at 373 K, which was close to the green colour of the unreacted olivine particle, also indicating that there was little Fe_2O_3 formed on the particle surface, compared with the two higher temperatures.

4.2.3. Comparisons

To compare the reaction between different temperatures, Table 8 summarizes the comparisons of the amount of dissolved olivine m_{diss}, the concentration of Fe in the aqueous phase after the completion of the reaction c_{add}(Fe) (where measured) and the molar percentage of Fe_2O_3 x_{Fe2O3} or SiO_2 x_{SiO2} present on the surface of the reacted olivine particles among different experiments. x_{Fe2O3} and x_{SiO2} were obtained by peak fitting the spectra O 1s, and/or the spectra Si 2p, given that the binding energies of O 1s are (531.09 ± 0.30) eV for olivine, (529.64 ± 0.72) eV for Fe_2O_3, and (532.94 ± 0.85) eV for SiO_2. Note that c_{add}(Fe) was the concentration of Fe from the liquid sample collected directly from reactor 2 using a pipettor at the conclusion of the experiment, after reactor 2 was opened, so this sample did not pass through the sampling system.

Table 8 shows that the amount of dissolved olivine was higher at 423 K (0.023 to 0.057 g) and 373 K (0.027 to 0.041 g), while that was lower at 473 K (0.008 to 0.02 g). The concentration of Fe in the aqueous phase after the completion of the reaction c_{add}(Fe) was the highest at 373 K (10^{-2} mmol·l^{-1}), at an intermediate level at 423 K (10^{-3} mmol·l^{-1}), and the lowest at 473 K (10^{-4} mmol·l^{-1}). The molar percentages of Fe_2O_3 x_{Fe2O3} on the surface of olivine particles were the highest (between 52 % and 60 %) at 423 K, were somewhat lower (between 37 % and 58 %) at 473 K, and were the lowest (≤ 10 %) at 373 K. Table 7 shows that the colour of the reacted olivine particles was brown at 423 and 473 K, while that of the reacted olivine particles was slightly yellowish green at 373 K. At the two higher temperatures, the brown colour of the reacted olivine particles appeared darker at 423 K than at 473 K.

Based on the aforementioned comparison, because a higher amount of olivine was dissolved at 423 K than at 473 K, more Fe^{2+} was released from olivine particles, and a higher amount of Fe_2O_3 was formed on the surface of olivine particles afterwards, and hence the brown colour was more intense at 423 K than at 473 K. Even though the released Fe^{2+} in the aqueous phase was consumed, c_{add}(Fe) was higher at 423 K than at 473 K. At 373 K, because only little Fe_2O_3 was formed on the surface of olivine particles, as indicated by the yellowish green colour of the reacted olivine particles and low values of x_{Fe2O3} (≤ 10 %) at this temperature, the released Fe^{2+} into the aqueous phase accumulated overtime, so the highest level of c_{add}(Fe) was observed at this temperature. The rising trend of c(Fe) as a function of reaction time shown in Fig. 12 also indicated the accumulation of Fe^{2+} in the solution.

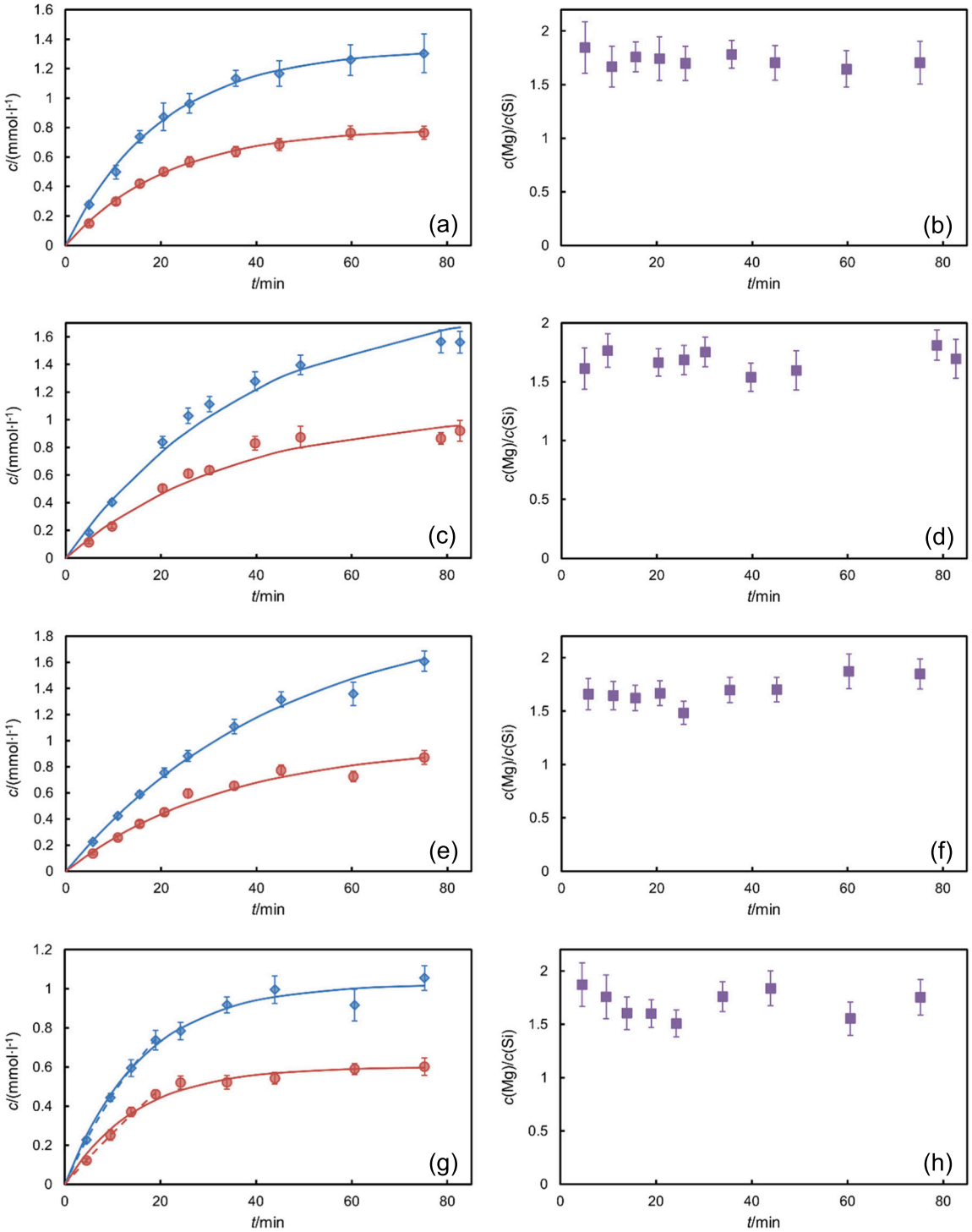


Fig. 11. Concentration c profiles of Mg and Si as a function of reaction time t at 373 K and at (a) $p_{CO2} = 15.6$ MPa (E-373-HP), (c) $p_{CO2} = 15.6$ MPa (E-373-HP-R), which is a repeated run with not fully stable stirring, (e) $p_{CO2} = 10.6$ MPa (E-373-MP), and (g) $p_{CO2} = 7.7$ MPa (E-373-LP). ◆, Mg; ●, Si; —, fitting curves for all data; - - -, fitting curves for initial periods to better represent the initial dissolution rate when overall fitting did not capture it accurately. Concentration ratio profiles between c(Mg) and c(Si) as a function of reaction time t at 373 K and at (b) $p_{CO2} = 15.6$ MPa (E-373-HP), (d) $p_{CO2} = 15.6$ MPa (E-373-HP-R), which is a repeated run with not fully stable stirring, (f) $p_{CO2} = 10.6$ MPa (E-373-MP), and (h) $p_{CO2} = 7.7$ MPa (E-373-LP).

For SiO_2 formation, while more SiO_2 (between 18 % and 34 %) was present on the surface of olivine particles at 373 K, 13 % and 10 % of SiO_2 was formed on the surface of olivine particles for E-423-HP and E-423-LP. Only no more than 6 % of SiO_2 was detected on the surface of olivine particles for the rest experiments. These values agreed with the XPS analysis of spectra Si 2p and O 1s earlier.

Therefore, it was concluded that Fe_2O_3 was the primary passivation layer formed at 423 and 473 K, whereas SiO_2 was the main passivation layer formed at 373 K.

As shown in Figs. 7, 9 and 11, while c(Mg) and c(Si) either approached near-equilibrium state or their increases slowed down within the 80-minute reaction at 373 and 473 K. The c(Mg) and c(Si) were far from equilibrium within the reaction time at 423 K, suggesting that 423 K was the optimum temperature for olivine dissolution in the

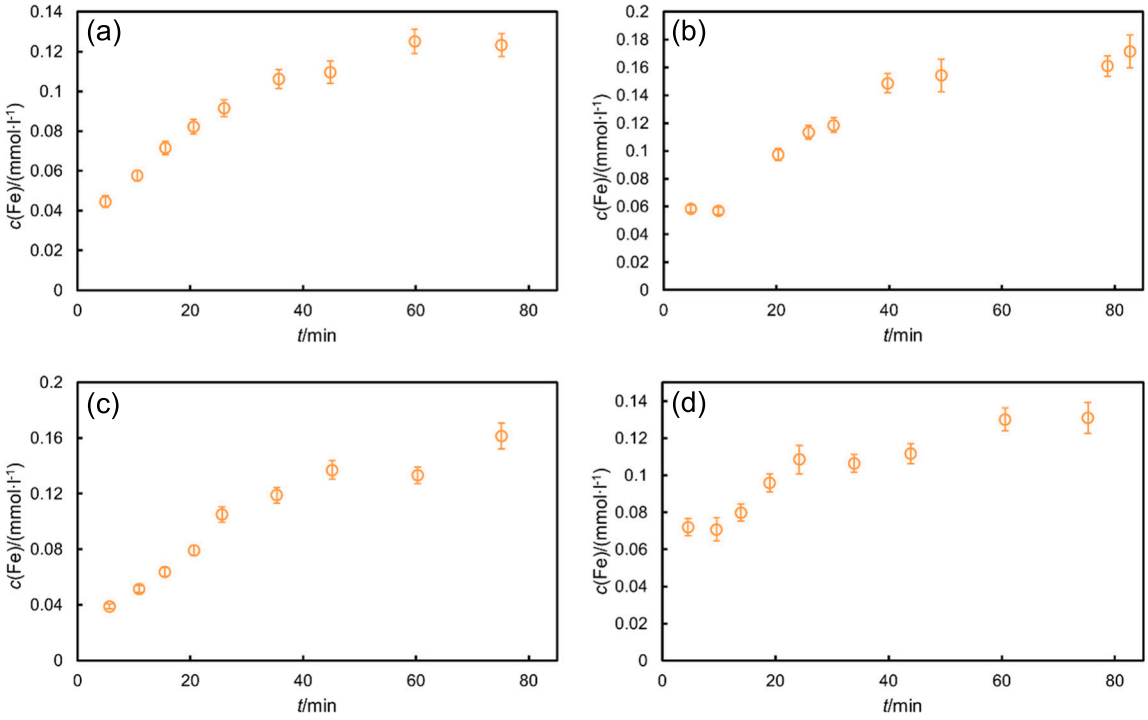


Fig. 12. Concentration c profiles of Fe as a function of reaction time t at 373 K and at (a) $p_{CO2} = 15.6$ MPa (E-373-HP), (b) $p_{CO2} = 15.6$ MPa (E-373-HP-R), which is a repeated run with not fully stable stirring, (c) $p_{CO2} = 10.6$ MPa (E-373-MP), and (d) $p_{CO2} = 7.7$ MPa (E-373-LP).

Table 8
The comparisons of the amount of dissolved olivine m_{diss}, the concentration of Fe in the aqueous phase after the completion of the reaction c_{add}(Fe) and the molar percentage of Fe_2O_3 x_{Fe2O3} or SiO_2 x_{SiO2} present on the surface of the reacted olivine particles among different experiments with a reaction time t_{total}.

Experiment	t_{total}/min	m_{diss}/g	$u(m_{diss})$/g	c_{add}(Fe)/(mmol·l^{-1})	$u[c_{add}(Fe)]$/(mmol·l^{-1})	x_{Fe2O3} [a]	x_{SiO2} [b]
E-473-HP-105	75.30	0.0092	0.0004	0.00049	0.00015	58	2
E-473-HP-120	74.88	0.0080	0.0002	0.00060	0.00036	47	2
E-473-MP	75.60	0.0136	0.0003	0.00016	0.00006	44	6
E-473-LP	75.30	0.0195	0.0005	0.00164	0.00038	37	5
E-423-HP	74.10	0.0289	0.0017	0.00014	0.00005	52	13
E-423-MP	54.18	0.0570	0.0018	0.00576	0.00564	60	4
E-423-LP	74.65	0.0517	0.0014	0.00268	0.00058	54	10
E-423-LP-R	75.28	0.0227	0.0007			56	5
E-373-HP	75.18	0.0344	0.0020	0.02778	0.00122	7	34
E-373-HP-R	82.70	0.0414	0.0021	0.07836	0.00346	6	18
E-373-MP	75.18	0.0408	0.0016	0.04108	0.00182	10	33
E-373-LP	75.22	0.0275	0.0013	0.09042	0.00582	9	29

[a] The standard relative uncertainty of x_{Fe2O3} is $u_r(x_{Fe2O3}) \leq 7$ %.
[b] The standard relative uncertainty of x_{SiO2} is $u_r(x_{SiO2}) \leq 7$ %.

long term.

4.2.4. Olivine initial dissolution rates

The olivine initial stoichiometric dissolution rates at different temperatures T and different pressures p_{CO2} are summarized in Table 9.

Some repeated measurements (E-373-HP-R and E-423-LP-R) were performed, but the olivine dissolution rate was not identical between these duplicates due to the bad performance of the stirring system (E-373-HP-R) or inconsistent performance of the stirring system between one measurement (E-423-LP-R) and the rest measurements. The olivine dissolution rate for the repeated measurement E-373-HP-R performed at $T = 373$ K and $p_{CO2} = 15.6$ MPa deviated by approximately 18 % from the other measurement E-373-HP conducted at the same temperature and pressure. The olivine dissolution rate for the repeated measurement E-423-LP-R conducted at $T = 423$ K and $p_{CO2} = 7.7$ MPa was about 2.8 times lower that for the measurement E-423-LP conducted at the same temperature and pressure.

4.2.5. Effects of temperature and passivation layer on olivine dissolution rate

The initial stoichiometric dissolution rate with respect to Mg and Si as a function of temperature T is plotted in Fig. 13. The olivine dissolution rate as a function of temperature T is shown in Fig. 13. With the increase of temperature, the olivine dissolution rate decreased first and then increased.

As discussed earlier, SiO_2 was mainly formed on the surface of olivine particles at 373 K, while Fe_2O_3 was mainly formed on the surface of olivine particles at 423 and 473 K. Because no more than 10 % of Fe_2O_3 was formed on the particle surface at 373 K, the initial decrease of dissolution rate from 373 to 423 K indicated that this decrease was dominated by Fe_2O_3 passivation layer formation. The increase of dissolution rate from 423 to 473 K was dominated by the kinetics of the olivine dissolution reaction itself, even though more Fe_2O_3 was formed at 423 K (52 % to 60 %) than at 473 K (37 % to 58 %). It was also concluded that Fe_2O_3 had a stronger inhibition than SiO_2 on olivine

Table 9
Olivine initial stoichiometric dissolution rate $r_{stoi,x}$ (x = Mg or Si) with standard uncertainty $u(r_{stoi,x})$, and average dissolution rate r_{Oliv} with standard uncertainty $u(r_{Oliv})$ at different temperatures T with standard uncertainty $u(T)$ and different pressures p_{CO2} with standard uncertainty $u(p_{CO2})$.

T	p_{CO2}	$10^7\ r_{stoi,Mg}$	$10^7\ u(r_{stoi,Mg})$	$10^7\ r_{stoi,Si}$	$10^7\ u(r_{stoi,Si})$	10^7 r_{Oliv}	$10^7\ u(r_{Oliv})$
K	MPa	$(mol{\cdot}m^{-2}{\cdot}s^{-1})$		$(mol{\cdot}m^{-2}{\cdot}s^{-1})$		$(mol{\cdot}m^{-2}{\cdot}s^{-1})$	
373.0	15.6	13.0	2.8	13.0	2.3	13.0	1.8
373.0 [a]	15.6	10.3	1.9	11.6	2.4	11.0	1.5
422.8	15.6	2.8	0.6	2.9	0.3	2.9	0.3
472.6 [b]	15.6	9.1	1.4	9.5	2.1	9.3	1.2
373.0	10.8	9.4	1.0	8.8	0.7	9.1	0.6
423.1	10.6	5.9	0.5	7.4	0.8	6.7	0.5
472.8	10.5	33.4	3.7	43.2	9.3	38.3	5.0
373.1	7.7	11.7	1.3	10.8	0.8	11.3	0.8
422.9	7.7	5.8	0.3	6.7	0.4	6.3	0.3
422.8 [c]	7.7	2.4	0.2	2.0	0.3	2.2	0.2
472.9	7.7	25.8	3.0	24.6	3.3	25.2	2.2

[a] Repeated measurement E-373-HP-R at T = 373 K and p_{CO2} = 15.6 MPa, stirring was not fully stable throughout the measurement.
[b] Values were taken the average of measurements E-473-HP-120 at ω = 120 s^{-1} and E-473-HP-105 at ω = 105 s^{-1}, at T = 473 K and p_{CO2} = 15.6 MPa in Table 2.
[c] Repeated measurement E-423-LP-R at T = 423 K and p_{CO2} = 7.7 MPa with stirring performed differently compared to the rest experiments.

dissolution because the dissolution rates at 373 K were higher than those at 423 K.

4.2.6. *Effects of CO2 pressure and passivation layer on olivine dissolution rate*

The effect of CO_2 pressure on olivine dissolution rate was considered to be mediated though the *p*H. The *p*H of CO_2-saturated water was obtained using *PHREEQC* with the Lawrence Livermore National Laboratory (llnl) database and is shown in Fig. 14. The *p*H plotted here refers to the *p*H of the system prior to olivine dissolution.

At the same temperature, the *p*H only decreased by 0.15 units for 373 K, 0.16 units for 423 K and 0.17 units for 473 K, with p_{CO2} increased from 7.7 to 15.6 MPa. The initial stoichiometric dissolution rate as a function of pressure p_{CO2} is plotted in Fig. 15. Pressure had little effect on olivine dissolution rate until the temperature was increased to 473 K. At 473 K, the dissolution rate was lowest at p_{CO2} = 15.6 MPa, higher at p_{CO2} = 10.6 MPa and the highest at p_{CO2} = 7.7 MPa. This trend in dissolution rates inversely corresponded to the molar percentage of Fe_2O_3 formed on the particle surface after the completion of the reaction. As shown in Table 8, the highest molar percentage of Fe_2O_3 was observed at the highest p_{CO2} = 15.6 MPa (58 % for E-473-HP-105 and 47 % for E-473-HP-120), followed by 44 % at p_{CO2} = 10.6 MPa, and the lowest percentage (37 %) at p_{CO2} = 7.7 MPa. Therefore, it was inferred that for E-473-HP-105 and E-473-HP-120 at p_{CO2} = 15.6 MPa, at the initial stage of reaction, Fe_2O_3 was formed more rapidly to cover a greater proportion of the reactive surface of olivine particles, leading to the lowest dissolution rate, compared with E-473-MP and E-473-LP.

At 423 K, similar percentages of Fe_2O_3 (52 % to 60 %) were present on the particle surface after the completion of reaction. Likewise, at 373 K, comparable percentages of SiO_2 (18 % to 34 %) were detected on the particle surface after the reaction. Therefore, it can be inferred that during the early stages of the reaction, similar amounts of Fe_2O_3 and SiO_2 were formed on the particle surface at 423 K and 373 K, respectively, leading to comparable initial dissolution rates across varying

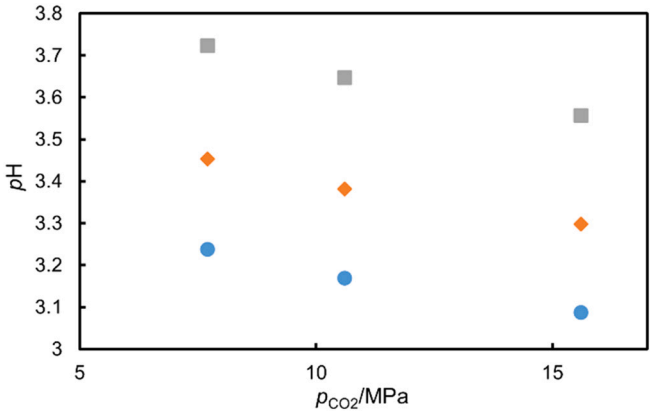


Fig. 14. *p*H of CO_2-saturated water as a function of CO_2 pressure p_{CO2}. ●, T = 373 K; ◆, T = 423 K; ■, T = 473 K.

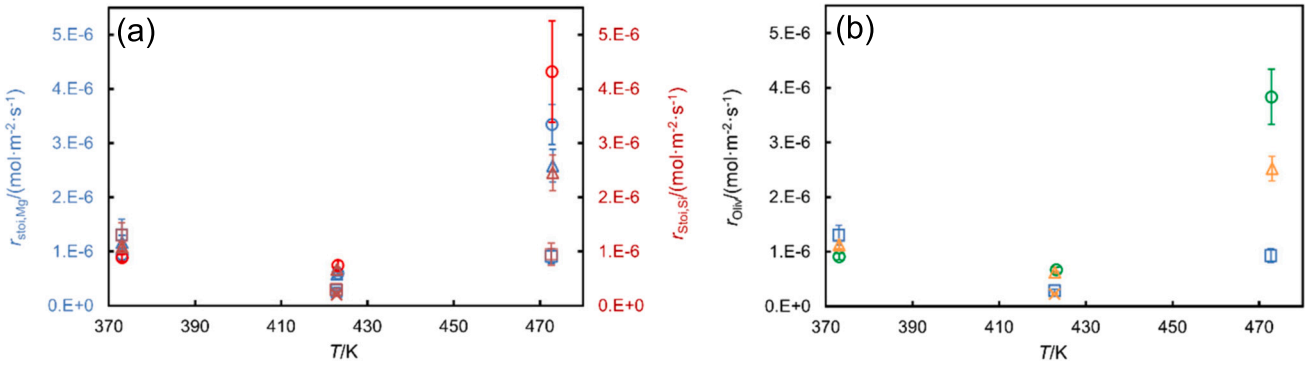


Fig. 13. (a) Olivine initial stoichiometric dissolution rate $r_{stoi,x}$ (x = Mg or Si) as a function of temperature T. □, p_{CO2} = 15.6 MPa; ○, p_{CO2} = 10.6 MPa; Δ, p_{CO2} = 7.7 MPa; ×, repeated measurement E-423-LP-R at p_{CO2} = 7.7 MPa and T = 423 K. Colour codes: blue, Mg; red, Si. (b) olivine dissolution rate r_{Oliv}, which was taken the average of $r_{stoi,Mg}$ and $r_{stoi,Si}$, as a function of temperature T. □, p_{CO2} = 15.6 MPa; ○, p_{CO2} = 10.6 MPa; Δ, p_{CO2} = 7.7 MPa; ×, repeated measurement E-423-LP-R at p_{CO2} = 7.7 MPa and T = 423 K.

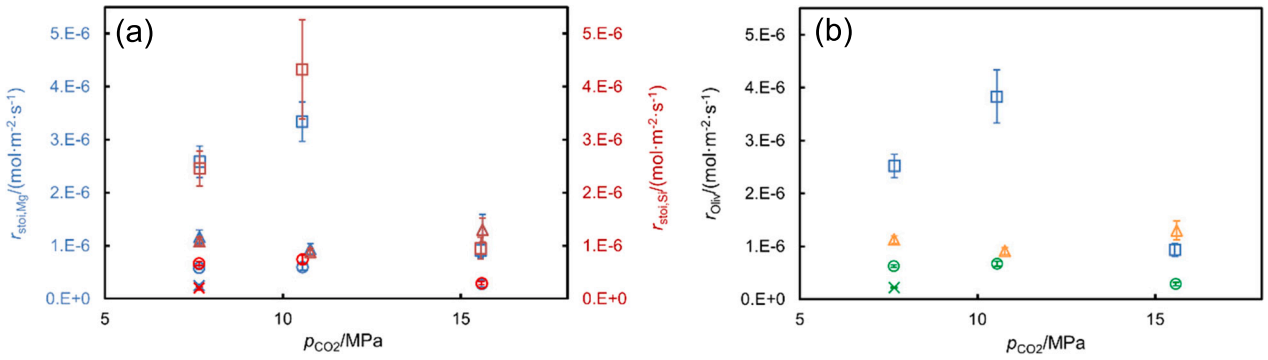


Fig. 15. (a) Olivine initial stoichiometric dissolution rate $r_{stoi,x}$ (x = Mg or Si) as a function of pressure p_{CO2}. □, T = 473 K; ○, T = 423 K; Δ, T = 373 K; ×, repeated measurement E-423-LP-R at p_{CO2} = 7.7 MPa and T = 423 K. Colour codes: blue, Mg; red, Si. (b) Olivine dissolution rate r_{Oliv}, which was taken the average of $r_{stoi,Mg}$ and $r_{stoi,Si}$, as a function of pressure p_{CO2}. □, T = 473 K; ○, T = 423 K; Δ, T = 373 K; ×, repeated measurement E-423-LP-R at p_{CO2} = 7.7 MPa and T = 423 K.

pressures at each temperature. This suggested that for ex-situ mineralization, very high pressures are not necessary.

4.2.7. Summary

In summary, Fe_2O_3 was the primary passivation layer formed at 423 and 473 K, whereas SiO_2 was the main passivation layer formed at 373 K. 423 K was the optimum temperature for olivine dissolution in the long term, because compared with 373 and 473 K, the concentrations of Mg and Fe were far from equilibrium within the reaction time at 423 K.

The initial olivine dissolution rate initially decreased and then increased with the increase of temperature when the CO_2 pressure was fixed. The decrease of initial olivine dissolution rates from 373 to 423 K was passivation dependent, which indicated that the ferric oxide formed on the olivine particle surface had a stronger inhibition on the initial olivine dissolution compared with silica. The increase of initial olivine dissolution rates from 423 to 473 K was dominated by the kinetics of the dissolution reaction itself. The influence of CO_2 pressure on initial olivine dissolution rates was slight until the temperature was increased to 473 K.

4.3. Modelling

According to the XPS analysis of recovered reacted olivine particles in Section 4.2, during olivine dissolution, Fe_2O_3 and/or SiO_2 formed as passivation layers on the surface of olivine particles. The dissolution of olivine in CO_2-saturated water is illustrated by Eqs. (1), (2) and (12). The formation of Fe_2O_3 is illustrated by Eqs. (13)–(15). The formation of SiO_2 is illustrated by Eq. (F.2). The formation of passivation layers reduced the reactive surface of olivine particles to some extent. To account for the inhibition effects of passivation layer, four methods were attempted to model the initial olivine dissolution rates r_{Oliv}, which was taken the average of $r_{stoi,Mg}$ and $r_{stoi,Si}$, as indicated in Eq. (9). Methods 1 to 3 are presented in Supplementary information SI J. The three methods failed to fit the experimental data.

Finally, a simplified temperature dependent term was introduced to represent the reactive fraction, reflecting the remaining reactivity of olivine in the presence of SiO_2 and Fe_2O_3 across all temperature conditions. The rate equation is given by

$$r = A_{Oliv} e^{\frac{-E_{a,Oliv}}{RT}} a_{H^+}^{n_{H^+}} \left\{ 1 - \frac{a}{1 + \exp\left[-b(T - T_p) \right]} \right\}, \quad (17)$$

where A_{Oliv} is the pre-exponential factor and activation energy for olivine dissolution, $E_{a,Oliv}$ is the activation energy for olivine dissolution, and a value of 70.4 kJ·mol^{-1} [28] was used for $E_{a,Oliv}$. R is gas constant, T is temperature, a_{H^+} is the activity of H^+, which was calculated by *PHREEQC* with the llnl database, n_{H^+} is the reaction order of H^+, a is the maximum inhibition effect, b is the steepness of the temperature dependence, and T_p is the reference temperature relevant to the inhibition caused by passivation layers. The term in braces can be interpreted as the reactive fraction or the fraction of the surface unpassivated and available for dissolution.

The fitting parameters in Eq. (17) (method 4) are summarized in Table 10. T_p was pre-determined prior to fitting. T_p was determined based on the experimental observations that (1) SiO_2 was the primary passivation layer formed at 373 K, while Fe_2O_3 was the dominant passivation layers formed at 423 and 473 K, and (2) Fe_2O_3 had a stronger inhibition than SiO_2 on olivine dissolution.

Constraints were applied to A_{Oliv} ($800 \leq A_{Oliv} \leq 10^6$) and n_{H^+} ($0.4 \leq n_{H^+} \leq 0.7$), based on the reported values for olivine dissolution [16–19,24,25,28,29], but large standard uncertainties were observed for both parameters. This was because the data were available at only three temperatures, while four fitting parameters needed to be determined, leading to an underdetermined problem. Nevertheless, compared with the first three methods, Eq. (17) with the fitting parameters listed in Table 10 provided a reasonable representation of the experimental data. Eq. (17) was an empirical interpolation model developed to correlate the limited experimental dataset obtained in the present work at the studied temperatures (373, 423 and 473 K) and CO_2 pressures (7.7, 10.6 and 15.6 MPa), with the consideration of different types of passivation layer. The effect of CO_2 pressure was incorporated into the model through its influence on *p*H. As such, the model is generally applicable under similar temperature and pressure conditions, and when the same type of passivation layer is present.

The experimental data and the fitting curves are shown in Fig. 16. As shown in Fig. 16(a), at the same CO_2 pressure, r_{Oliv} decreased between 373 and 423 K, whereas it increased between 423 and 473 K, aligning with the experimental results. Note that dashed curves were used to connect the two r_{Oliv} values at 373 and 423 K only, as the predicted r_{Oliv} between 373 and 423 K, excluding 373 and 423 K, cannot be validated by the experimental results. This was because SiO_2 was the main passivation layer formed at 373 K, whereas Fe_2O_3 was the primary passivation layer formed at 423 K. However, the temperature at which

Table 10
Fitting parameters with standard uncertainty u in Eq. (17).

$E_{a,Oliv}$/ (kJ·mol^{-1})	A_{Oliv}/ (mol·m^{-2}·s^{-1})	$u(A_{Oliv})$/ (mol·m^{-2}·s^{-1})	n_{H^+}	$u(n_{H^+})$	a	$u(a)$	b /K^{-1}	$u(b)$ /K^{-1}	T_p /K
70.4 [28]	141,069	1,239,268	0.4	1.37	0.97	0.04	600	0	373.15

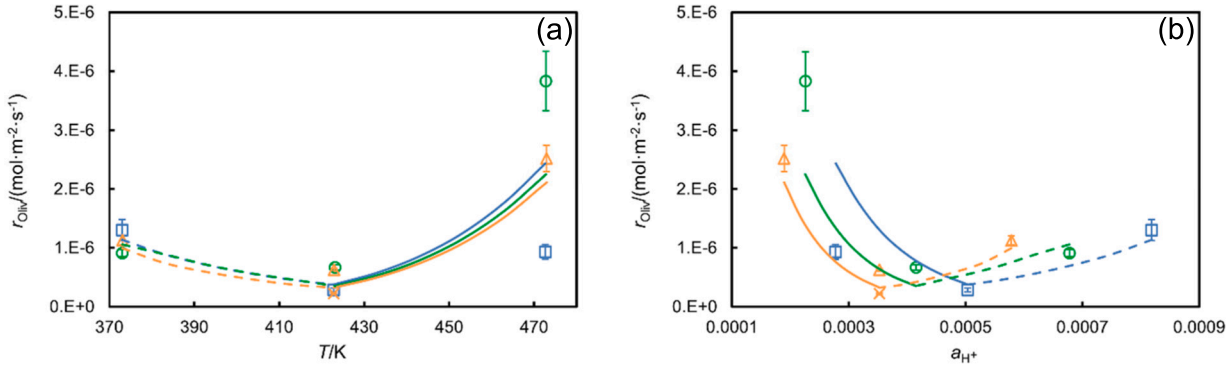


Fig. 16. Olivine dissolution rate r_{Oliv}, which was taken the average of $r_{stoi,Mg}$ and $r_{stoi,Si}$, (a) as a function of temperature T, and (b) as a function of the activity of H^+ a_{H^+}. □, p_{CO2} = 15.6 MPa; ○, p_{CO2} = 10.6 MPa; Δ, p_{CO2} = 7.7 MPa; ×, repeated measurement E-423-LP-R at p_{CO2} = 7.7 MPa and T = 423 K; solid curves: —, model from Eq. (17) with fitting parameters given in Table 10. Colour codes for solid curves: blue, 15.6 MPa; green, 10.6 MPa; orange, 7.7 MPa.

the dominant passivation layer changed remained unknown. Hence, additional data between these two temperatures would be required to refine the model. On the other hand, because Fe_2O_3 remained the dominant passivation layer at 423 and 473 K, the predicted r_{Oliv} between this range was more reliable. The average absolute relative deviations (AARD) of r_{Oliv} were (14 %, 43 % and 73 %) at T = (373, 423 and 473) K, respectively, as shown in Fig. K.1 in Supplementary information SI K. Large deviations were observed at 473 K.

Hänchen et al. [24] obtained a correlation in the form of Eq. (7) for the dissolutions rate of olivine based on their experiment results in CO_2-free solutions at temperatures between 363 and 423 K. Similarly, Rimstidt et al. [28] proposed a model of the same form as Eq. (7) for olivine dissolution rates at temperatures between 273 and 423 K based on an extended dataset from the literature. There was only one previous dataset on Olivine dissolution rate at 423 K reported by Hänchen et al. [24]. Besides the eight dissolution rates obtained in CO_2-free solutions from Hänchen et al. [24], Rimstidt et al. [28] also included two data points obtained in the presence of CO_2, from Hänchen et al. [24], to parameterize Eq. (7).The fitting parameters for Eq. (7) determined by Hänchen et al. [24] and Rimstidt et al. [28] are summarized in Table K.1. Fig. K.2 compares the olivine dissolution rates predicted by the correlation with the parameters listed in Table K.1, and the olivine dissolution rates determined in this study, at 373 and 423 K. The olivine dissolution rates predicted by both correlations increased with the increase of temperature.

At 373 K, the dissolution rates predicted by the two correlations closely matched the rates determined in this study, while at 423 K, the predicted rates were substantially higher than those determined experimentally in this study, suggesting that the inhibition effect of distinct primary passivation layers formed at different temperatures were not captured by these correlations. It is important to note that the predictions at 423 K from both correlations were based on the experimental data reported by Hänchen et al. [24], which represents the only available dataset for Olivine dissolution rates at this temperature in the literature. The AARD of r_{Oliv} between the olivine dissolution rates determined in this study and predicted by the models proposed by Hänchen et al. [24] and Rimstidt et al. [28] were 11 % and 23 %, respectively, at T = 373 K. However, at T = 423 K, compared with the same models, r_{Oliv} deviated by a factor of 18 and 26, respectively.

The large deviations observed at 423 K were attributed to the differences between the experiments in this study and those performed by Hänchen et al. [24], as summarized in Table K.2. No iron-oxide layer was visually observed on the recovered olivine particle surface by Hänchen et al. [24], whereas Fe_2O_3 was detected on the recovered olivine particle surface in this study. The key reason for this discrepancy was attributed to the differences in experimental methods. Hänchen et al. [24] conducted flow-through experiments, in which liquids were continuously injected and withdrawn at the same rate. As a result, the Fe^{2+} released from olivine particles was steadily removed from the reactor, making it more difficult to reach supersaturation with respect to $Fe(OH)_3$, which is the intermediate in the formation of Fe_2O_3. Furthermore, the continuous flushing of olivine particles with fresh solution created strong liquid convection, which inhibited the formation of iron oxide passivation layers on the particle surfaces. On the other hand, in this study, batch reactor experiments were performed, which allowed the released Fe^{2+} to accumulate in the solution, which significantly increased the likelihood of reaching $Fe(OH)_3$ supersaturation, thereby promoting the formation of Fe_2O_3 on the surface of olivine particles. The dissolution rates at 423 K reported by this work were about 0.5 to 2 orders of magnitude lower than those reported by Hänchen et al. [24], due to the formation of the iron oxide passivation layer.

The formation of a ferric iron-rich layer has also been reported in several other studies. Chen and Brantley [16] observed the presence of a ferric iron rich-layer on the olivine surface in open-air batch reaction experiments at 338 K. King et al. [74] detected the formation of hematite in unstirred batch reaction experiments on olivine carbonation in $NaHCO_3$ and NaCl brines at temperatures between 353 and 473 K. Sissmann et al. [75] reported the formation of a ferric iron-rich phase in batch experiments on olivine carbonation in pure water at a CO_2 pressure of 28 MPa and temperatures of 393 and 443 K. Saldi et al. [76,77] observed the formation of a ferric iron-rich layer on olivine surface in batch reaction experiments and mixed-flow experiments on olivine carbonation in pure water at 423 K and a CO_2 pressure of 10 MPa under oxic conditions. A common conclusion across these studies and the present work was that the formation of the ferric iron-rich layer slows down olivine dissolution, thereby hindering the carbonation process.

A common feature of these studies and the present work was that the ions such as Fe^{2+} released from olivine were able to accumulate in the solution because of the experimental methods: batch reaction experiments and mixed flow reaction experiments. As a result, the supersaturation state with respect to $Fe(OH)_3$ was more likely to occur, hence facilitating the formation of the ferric iron-rich layer on the surface of olivine particles. This significantly differed from the experimental method used by Hänchen et al. [24], in which the released ions were continuously removed from the solution, preventing the formation of ferric iron-rich phase.

Another distinction between this work and Hänchen et al. [24] was the experimental conditions. Among the ten olivine dissolution data points at 423 K reported by Hänchen et al. [24], eight were obtained under N_2 atmosphere with added HCl, and only two were conducted in the presence of CO_2. Hänchen et al. [24] parameterized Eq. (7) using only the dissolution rate data obtained under N_2 atmosphere, whereas Rimstidt et al. [28] incorporated all ten data points reported by Hänchen et al. [24], including the two obtained in the presence of CO_2, when developing their correlation. On the other hand, all dissolution rate data in this study were collected under CO_2-rich conditions.

PHREEQC modelling of olivine dissolution in CO_2-saturated water at temperatures of 373, 423 and 473 K and CO_2 pressures of 15.6, 10.6 and 7.7 MPa was performed using the llnl database. To model olivine dissolution for a period of time, besides the temperature and the activity of H^+ considered in Eq. (17), the total surface area S_t of olivine particles and the effect of saturation state on reaction rate were also accounted for. Accordingly, the olivine dissolution rate is given by

$$r_t = S_t A_{\mathrm{Oliv}} e^{\frac{-E_{a,\mathrm{Oliv}}}{RT}} a_{H^+}^{n_{H^+}} \left\{ 1 - \frac{a}{1 + \exp\left[-b\left(T - T_p\right) \right]} \right\} f(\Delta G_r), \tag{18}$$

where r_t is overall olivine dissolution rate at a given total surface area S_t, and $f(\Delta G_r)$ is the rate dependence as a function of the Gibbs free energy of olivine dissolution.

Assuming the olivine particles have a spherical shape and dissolution proceeds uniformly, the changes in S during the reaction is approximated by [78].

$$S_t = S_{t,0} \left(\frac{m}{m_0} \right)^d, \tag{19}$$

where $S_{t,0}$ is initial total surface area, m_0 is initial total mass of olivine particles, m is total mass of olivine particles, and d is an exponent that depends on the geometry of particles and how surface area relates to mass during shrinkage. d usually varies between 2/3 and 1. For a single sphere, $d = 2/3$ [78]. d was adjusted to achieve a close match between the predicted concentrations and measured concentrations.

For the term $f(\Delta G_r)$ that accounted for the effect of saturation state on reaction rate, one of the commonly used forms is given by [73,79–83].

$$f(\Delta G_r) = [1 - (Q/K)^p]^q, \tag{20}$$

where Q is the reaction quotient, K is the equilibrium constant, and p and q are empirical fitting parameters, which are dimensionless.

Therefore, Eq. (18) is given by

$$r_t = S_{t,0} \left(\frac{m}{m_0} \right)^d A_{\mathrm{Oliv}} e^{\frac{-E_{a,\mathrm{Oliv}}}{RT}} a_{H^+}^{n_{H^+}} \left\{ 1 - \frac{a}{1 + \exp\left[-b\left(T - T_p\right) \right]} \right\} [1 - (Q/K)^p]^q. \tag{21}$$

Eq. (21) was used in *PHREEQC* modelling.

The concentration c profiles of Mg, Si, Fe, the pH profiles, and the saturation indices of hematite, goethite (FeO(OH)), $Fe(OH)_3$, quartz and amorphous silica, as a function of reaction time at 473 K, 423 K and 373 K are shown in Figs. K.3, K.4 and K.5, respectively. Note that the measured concentrations of Fe included the contamination from the system as discussed in section Supplementary information SI D, and therefore comparisons between the predicted and measured concentrations of Fe were not made. Table K.3 summarizes the values of the fitting parameters used in *PHREEQC* modelling for a good fit for various experimental results.

At 473 and 423 K, the predicted saturation index of hematite (Fe_2O_3) alone, or of both hematite (Fe_2O_3) and goethite (FeO(OH)) became positive during the reaction, which was consistent with the experimental observation that Fe_2O_3 was the primary passivation layer formed at these temperatures. At 473 K, the predicted concentrations of Mg and Si matched the experimental data only at the very beginning in all cases. This was because the difficulty in accurately modelling the inhibition effects of Fe_2O_3 and/or FeO(OH) formation on the olivine particle surface using *PHREEQC*, especially in these cases where Fe_2O_3 and FeO(OH) formed from the onset of the reactions. In contrast, at 423 K, the predicted Mg and Si concentrations matched the experimental data throughout the reaction, suggesting that model properly captured the olivine dissolution behaviour including the inhibition caused by Fe_2O_3 at 423 K.

At 373 K, in the prediction where the predicted concentrations of Mg and Si aligned more closely with the measured data during the early stages of the reaction, the predicted saturation index of quartz was initially negative but became positive as the reaction progressed. This was consistent with the experimental observations that SiO_2 was the primary passivation layer formed at 373 K. However, the *PHREEQC* modelling failed to account for the inhibition of SiO_2 formation on the olivine particle surface at 373 K, leading to an overestimation of the predicted concentrations during the later stages of the reaction.

5. Conclusions

In this study, the dissolution kinetics of olivine in CO_2-saturated water at temperatures between 373 and 473 K and at pressures between 7.7 and 15.6 MPa, which are of relevance to in-situ and ex-situ carbon mineralization conditions, have been studied. Batch reaction experiments on olivine dissolution were conducted. The apparent initial olivine dissolution rates were determined by measuring the concentrations of Mg, Si and Fe in the liquid samples using ex-situ ICP-MS and/or ICP-OES. Although these represented initial reaction rates, the reported values still reflected the reaction process including the formation of passivation layers and their inhibition effects over a period of time in which the concentration profiles of Mg and Si were fitted. The recovered reacted olivine particles were analysed by ex-situ XPS, ToF-SIMS and SEM-EDX. The conclusions are as follows.

Passivation layers were formed on the olivine surface in parallel with olivine dissolution. Silica was the primary passivation layer formed at 373 K, while ferric oxide was the main passivation layer formed at 423 and 473 K. The formation of passivation layer such as iron oxide slows down Olivine dissolution, thereby hindering the carbonation process. The influence of mass transfer resistance on olivine dissolution was studied by varying the angular velocity of the stirrer in the batch reactor. With the increase of angular velocity, the initial olivine dissolution rate first decreased, then increased and eventually reached a plateau. Compared with olivine dissolution itself, the formation of the passivation layer was hindered more at low angular velocity. This was because the presence of a boundary layer between the olivine particle surface and the bulk solution introduced more diffusion steps for the transport of reactants required for passivation layer (Fe_2O_3) formation than for olivine dissolution. As a result, a fast net olivine dissolution rate was achieved at low angular velocity, which suggested that under reservoir conditions without stirring, the passivation layer would form only slowly, allowing more rapid olivine dissolution and hence releasing more Mg^{2+} for mineralization. On the other hand, SiO_2 and Fe_2O_3 formed during the process can potentially be recovered and utilized as valuable materials in ex-situ carbon mineralization.

By performing experiments at the angular velocity at which the mass transfer resistance was effectively eliminated, the apparent initial olivine dissolution rates at different temperatures and pressures were obtained. The initial olivine dissolution rate initially decreased and then increased with the increase of temperature when the CO_2 pressure was fixed. The decrease of initial olivine dissolution rates from 373 to 423 K was passivation dependent, which indicated that the ferric oxide formed on the olivine particle surface had a stronger inhibition on the initial olivine dissolution compared with silica. The increase of initial olivine dissolution rates from 423 to 473 K was dominated by the kinetics of the dissolution reaction itself. The influence of CO_2 pressure on initial olivine dissolution rates was slight until the temperature was increased to 473 K, which was because similar amounts of iron oxide and silica were formed on the olivine particle surface across all pressures at 423 K

and 373 K, respectively, leading to comparable initial dissolution rates across varying pressures at each temperature. At 473 K, ferric oxide likely formed more rapidly at 15.6 MPa than at 10.6 and 7.7 MPa, resulting in a lower initial olivine dissolution rate at 15.6 MPa. This suggested that for ex-situ mineralization, very high pressures are not necessary.

Compared with 373 and 473 K, the concentrations of Mg and Fe were far from equilibrium within the reaction time at 423 K, suggesting that 423 K was the optimum temperature for olivine dissolution in the long term.

This study provides the first data for olivine dissolution rates at temperatures above 423 K. An empirical interpolation model that was dependent upon temperature and the activity of H^+ was developed to represent the limited experimental dataset obtained in the present work at the studied temperatures (373, 423 and 473 K) and CO_2 pressures (7.7, 10.6 and 15.6 MPa), with the consideration of different types of passivation layer. The effect of CO_2 pressure was incorporated into the model through its influence on *p*H. As such, the model is generally applicable under similar temperature and pressure conditions, and when the same type of passivation layer is present. The model might be further refined with the help of additional experimental data between 373 and 423 K and below 373 K. Based on the proposed model, *PHREEQC* modelling was performed to predict the saturation indices of hematite (Fe_2O_3), goethite (FeO(OH)), $Fe(OH)_3$, quartz and amorphous silica, *p*H, and element concentrations to rationalize the experimental results.

For future work, to better understand the formation of the iron-rich passivation layer during olivine dissolution, it is essential to measure accurately the concentration of Fe in the liquid samples and this would require elimination of iron-containing wetted surfaces. This might be achieved via gold plating the surfaces of the reactor, or fitting a polytetrafluoroethylene (PTFE) liner, and by utilizing valves and tubing made of polymers such as polyaryletherketone (PAEK) and polyether ether ketone (PEEK). In this study, Fe_2O_3 was detected on the recovered reacted olivine particles that underwent reaction at 423 and 473 K. As discussed in Section 4.1.4, the possible processes for the oxidation of Fe^{2+} were: (1) Fe^{2+} was oxidized in-situ in the olivine particle; (2) Fe^{2+} was first released to the liquid, and was then oxidized, and finally Fe_2O_3 precipitated on the olivine particle surface; (3) both of the processes mentioned. Under the current operation procedures, only the second pathway for the oxidation of ferrous iron was confirmed, but the first pathway where ferrous iron was oxidized in-situ, could not be excluded. Therefore, to investigate if serpentinization occurred (resulting in H_2 production) alongside olivine dissolution by H^+ in CO_2-saturated water, gas sampling coupled with analysis by mass spectrometry or gas chromatography is recommended.

CRediT authorship contribution statement

Qiaoyun Chen: Writing – original draft, Validation, Methodology, Investigation, Formal analysis, Conceptualization. **J.P. Martin Trusler:** Writing – review & editing, Supervision, Resources, Funding acquisition, Conceptualization.

Declaration of competing interest

The authors declare the following financial interests/personal relationships which may be considered as potential competing interests: Qiaoyun Chen reports financial support was provided by China Scholarship Council. If there are other authors, they declare that they have no known competing financial interests or personal relationships that could have appeared to influence the work reported in this paper.

Acknowledgement

The Imperial-CSC Scholarship jointly funded by Imperial College London and the China Scholarship Council is acknowledged. We thank Prof. Ronny Pini for granting access to the Autosorb iQ instrument, and Dr. Hassan Azzan, Dr. Humera Ansari, and Mr. Killian Gmyrek for their assistance with the N_2 adsorption measurement.

Appendix A. Supplementary data

Supplementary data to this article can be found online at https://doi.org/10.1016/j.cej.2025.169095.

Data availability

Data will be made available on request.

References

[1] G. Gadikota, Carbon mineralization pathways for carbon capture, storage and utilization, Commun. Chem. 4 (1) (2021) 23, https://doi.org/10.1038/s42004-021-00461-x.
[2] S. Benson, P. Cook, J. Anderson, S. Bachu, H. Nimir, B. Basu, J. Anderson, G. Deguchi, J. Gale, G. von Goerne, W. Heidug, Underground geological storage, in: IPCC Special Report on Carbon Dioxide Capture and Storage, 2005.
[3] S.Ó. Snæbjörnsdóttir, B. Sigfússon, C. Marieni, D. Goldberg, S.R. Gislason, E. H. Oelkers, Carbon dioxide storage through mineral carbonation, Nat. Rev. Earth Environ. 1 (2) (2020) 90–102, https://doi.org/10.1038/s43017-019-0011-8.
[4] C. Julcour, F. Bourgeois, B. Bonfils, I. Benhamed, F. Guyot, F. Bodénan, C. Petiot, É. C. Gaucher, Development of an attrition-leaching hybrid process for direct aqueous mineral carbonation, Chem. Eng. J. 262 (2015) 716–726, https://doi.org/10.1016/j.cej.2014.10.031.
[5] J. Kang, Z. Yu, Y. Zhang, T. Xu, L. Guo, S. Hao, Optimization of CO2 sequestration in alkaline industrial residues: the enhancement mechanism of saline soil, Chem. Eng. J. 486 (2024) 150402, https://doi.org/10.1016/j.cej.2024.150402.
[6] F. Wang, D. Dreisinger, An integrated process of CO2 mineralization and selective nickel and cobalt recovery from olivine and laterites, Chem. Eng. J. 451 (2023) 139002, https://doi.org/10.1016/j.cej.2022.139002.
[7] F. Wang, D. Dreisinger, M. Jarvis, T. Hitchins, L. Trytten, CO2 mineralization and concurrent utilization for nickel conversion from nickel silicates to nickel sulfides, Chem. Eng. J. 406 (2021) 126761, https://doi.org/10.1016/j.cej.2020.126761.
[8] O. Bashir Wani, S. Khan, M. Shoaib, H. Zeng, E.R. Bobicki, Decarbonization of mineral processing operations: realizing the potential of carbon capture and utilization in the processing of ultramafic nickel ores, Chem. Eng. J. 433 (2022) 134203, https://doi.org/10.1016/j.cej.2021.134203.
[9] N. Zhang, R. Yang, H.D. Huang, J. Meng, W. Zhang, A.-H.A. Park, A. Moment, Integrated recovery of iron and nickel from olivine ores using solvent extraction: synergistic production of amorphous silica and carbonates through pH adjustment and carbon mineralization, ACS ES&T Eng. 5 (1) (2025) 103–114, https://doi.org/10.1021/acsestengg.4c00462.
[10] S.J. Gerdemann, W.K. O'Connor, D.C. Dahlin, L.R. Penner, H. Rush, Ex situ aqueous mineral carbonation, Environ. Sci. Technol. 41 (7) (2007) 2587–2593, https://doi.org/10.1021/es0619253.
[11] N.C. Johnson, B. Thomas, K. Maher, R.J. Rosenbauer, D. Bird, G.E. Brown, Olivine dissolution and carbonation under conditions relevant for in situ carbon storage, Chem. Geol. 373 (2014) 93–105, https://doi.org/10.1016/j.chemgeo.2014.02.026.
[12] T.J. Hassett, Equilibrium concepts in soil–the use of the CO_2-H_2O system in teaching equilibrium concepts, J. Agron. Educ. 2 (1) (1973) 68–72, https://doi.org/10.2134/jae.1973.0068.
[13] O. Pedersen, T.D. Colmer, K. Sand-Jensen, Underwater Photosynthesis of Submerged Plants – Recent Advances and Methods 4, 2013, https://doi.org/10.3389/fpls.2013.00140.
[14] S. Perez, J.-M. Etancelin, P. Poncet, A semi-Lagrangian method for the direct numerical simulation of crystallization and precipitation at the pore scale 13 (2025), https://doi.org/10.3389/feart.2025.1493305.
[15] A. Takolander, Assessing the Effects of Climate Change on Baltic Sea Macroalgae – Implications for the Foundation Species *Fucus vesiculosus* L, 2018.
[16] Y. Chen, S.L. Brantley, Dissolution of forsteritic olivine at 65°C and 2< pH< 5, Chem. Geol. 165 (3–4) (2000) 267–281.
[17] J.J. Rosso, J.D. Rimstidt, A high resolution study of forsterite dissolution rates, Geochim. Cosmochim. Acta 64 (5) (2000) 797–811, https://doi.org/10.1016/S0016-7037(99)00354-3.
[18] E.H. Oelkers, An experimental study of forsterite dissolution rates as a function of temperature and aqueous Mg and Si concentrations, Chem. Geol. 175 (3) (2001) 485–494, https://doi.org/10.1016/S0009-2541(00)00352-1.
[19] R.A. Wogelius, J.V. Walther, Olivine dissolution at 25°C: effects of *p*H, CO_2, and organic acids, Geochim. Cosmochim. Acta 55 (4) (1991) 943–954, https://doi.org/10.1016/0016-7037(91)90153-v.
[20] S.V. Golubev, O.S. Pokrovsky, J. Schott, Experimental determination of the effect of dissolved CO_2 on the dissolution kinetics of Mg and ca silicates at 25 °C, Chem. Geol. 217 (3) (2005) 227–238, https://doi.org/10.1016/j.chemgeo.2004.12.011.
[21] O.S. Pokrovsky, J. Schott, Kinetics and mechanism of forsterite dissolution at 25°C and pH from 1 to 12, Geochim. Cosmochim. Acta 64 (19) (2000) 3313–3325, https://doi.org/10.1016/s0016-7037(00)00434-8.

[22] D.E. Giammar, R.G. Bruant, C.A. Peters, Forsterite dissolution and magnesite precipitation at conditions relevant for deep saline aquifer storage and sequestration of carbon dioxide, Chem. Geol. 217 (3–4) (2005) 257–276, https://doi.org/10.1016/j.chemgeo.2004.12.013.
[23] F. Wang, D.E. Giammar, Forsterite dissolution in saline water at elevated temperature and high CO_2 pressure, Environ. Sci. Technol. 47 (1) (2013) 168–173, https://doi.org/10.1021/es301231n.
[24] M. Hänchen, V. Prigiobbe, G. Storti, T.M. Seward, M. Mazzotti, Dissolution kinetics of fosteritic olivine at 90–150°C including effects of the presence of CO_2, Geochim. Cosmochim. Acta 70 (17) (2006) 4403–4416, https://doi.org/10.1016/j.gca.2006.06.1560.
[25] V. Prigiobbe, G. Costa, R. Baciocchi, M. Hänchen, M. Mazzotti, The effect of CO_2 and salinity on olivine dissolution kinetics at 120°C, Chem. Eng. Sci. 64 (15) (2009) 3510–3515, https://doi.org/10.1016/j.ces.2009.04.035.
[26] V. Prigiobbe, M. Mazzotti, Dissolution of olivine in the presence of oxalate, citrate, and CO_2 at 90°C and 120°C, Chem. Eng. Sci. 66 (24) (2011) 6544–6554, https://doi.org/10.1016/j.ces.2011.09.032.
[27] D. Daval, O. Sissmann, N. Menguy, G.D. Saldi, F. Guyot, I. Martinez, J. Corvisier, B. Garcia, I. Machouk, K.G. Knauss, R. Hellmann, Influence of amorphous silica layer formation on the dissolution rate of olivine at 90°C and elevated pCO_2, Chem. Geol. 284 (1) (2011) 193–209, https://doi.org/10.1016/j.chemgeo.2011.02.021.
[28] J.D. Rimstidt, S.L. Brantley, A.A. Olsen, Systematic review of forsterite dissolution rate data, Geochim. Cosmochim. Acta 99 (2012) 159–178, https://doi.org/10.1016/j.gca.2012.09.019.
[29] R.A. Wogelius, J.V. Walther, Olivine dissolution kinetics at near-surface conditions, Chem. Geol. 97 (1) (1992) 101–112, https://doi.org/10.1016/0009-2541(92)90138-U.
[30] M.A. Saleh, H. Shiel, M.P. Ryan, J.P.M. Trusler, S. Krevor, Enhanced olivine reactivity in wet supercritical CO_2 for engineered mineral carbon sequestration, Energy Fuel 38 (21) (2024) 21028–21041, https://doi.org/10.1021/acs.energyfuels.4c04120.
[31] D.E. Clark, E.H. Oelkers, I. Gunnarsson, B. Sigfússon, S.Ó. Snæbjörnsdóttir, E. S. Aradóttir, S.R. Gíslason, CarbFix2: CO_2 and H_2S mineralization during 3.5 years of continuous injection into basaltic rocks at more than 250 °C, Geochim. Cosmochim. Acta 279 (2020) 45–66, https://doi.org/10.1016/j.gca.2020.03.039.
[32] S.R. Gíslason, H. Sigurdardóttir, E.S. Aradóttir, E.H. Oelkers, A brief history of CarbFix: challenges and victories of the project's pilot phase, Energy Procedia 146 (2018) 103–114, https://doi.org/10.1016/j.egypro.2018.07.014.
[33] S. Brunauer, P.H. Emmett, E. Teller, Adsorption of gases in multimolecular layers, J. Am. Chem. Soc. 60 (2) (1938) 309–319, https://doi.org/10.1021/ja01269a023.
[34] C. Peng, J.P. Crawshaw, G.C. Maitland, J.P.M. Trusler, Kinetics of calcite dissolution in CO_2-saturated water at temperatures between (323 and 373) K and pressures up to 13.8 MPa, Chem. Geol. 403 (2015) 74–85, https://doi.org/10.1016/j.chemgeo.2015.03.012.
[35] B. Malvoisin, F. Brunet, J. Carlut, S. Rouméjon, M. Cannat, Serpentinization of oceanic peridotites: 2. Kinetics and processes of San Carlos olivine hydrothermal alteration, journal of geophysical research: solid, Earth 117 (B4) (2012), https://doi.org/10.1029/2011JB008842.
[36] T.M. McCollom, F. Klein, M. Ramba, Hydrogen generation from serpentinization of iron-rich olivine on Mars, icy moons, and other planetary bodies, Icarus 372 (2022) 114754, https://doi.org/10.1016/j.icarus.2021.114754.
[37] B.W. Evans, K. Hattori, A. Baronnet, Serpentinite: what, why, where? Elements 9 (2) (2013) 99–106, https://doi.org/10.2113/gselements.9.2.99.
[38] S. Guillot, K. Hattori, Serpentinites: essential roles in geodynamics, arc volcanism, sustainable development, and the origin of life, Elements 9 (2) (2013) 95–98, https://doi.org/10.2113/gselements.9.2.95.
[39] H.M. Lamadrid, Z. Zajacz, F. Klein, R.J. Bodnar, Synthetic fluid inclusions XXIII. Effect of temperature and fluid composition on rates of serpentinization of olivine, Geochim. Cosmochim. Acta 292 (2021) 285–308, https://doi.org/10.1016/j.gca.2020.08.009.
[40] M. Andreani, I. Daniel, M. Pollet-Villard, Aluminum speeds up the hydrothermal alteration of olivine 98 (10) (2013) 1738–1744, https://doi.org/10.2138/am.2013.4469.
[41] R. Huang, M. Song, X. Ding, S. Zhu, W. Zhan, W. Sun, Influence of pyroxene and spinel on the kinetics of peridotite serpentinization, J. Geophys. Res. Solid Earth 122 (9) (2017) 7111–7126, https://doi.org/10.1002/2017JB014231.
[42] F. Klein, N.G. Grozeva, J.S. Seewald, T.M. McCollom, S.E. Humphris, B. Moskowitz, T.S. Berquó, W.-A. Kahl, Fluids in the crust. Experimental constraints on fluid-rock reactions during incipient serpentinization of harzburgite 100 (4) (2015) 991–1002, https://doi.org/10.2138/am-2015-5112.
[43] R. Lafay, G. Montes-Hernandez, E. Janots, R. Chiriac, N. Findling, F. Toche, Mineral replacement rate of olivine by chrysotile and brucite under high alkaline conditions, J. Cryst. Growth 347 (1) (2012) 62–72, https://doi.org/10.1016/j.jcrysgro.2012.02.040.
[44] R. Lafay, G. Montes-Hernandez, E. Janots, R. Chiriac, N. Findling, F. Toche, Simultaneous precipitation of magnesite and lizardite from hydrothermal alteration of olivine under high-carbonate alkalinity, Chem. Geol. 368 (2014) 63–75, https://doi.org/10.1016/j.chemgeo.2014.01.008.
[45] H.M. Lamadrid, J.D. Rimstidt, E.M. Schwarzenbach, F. Klein, S. Ulrich, A. Dolocan, R.J. Bodnar, Effect of water activity on rates of serpentinization of olivine, Nat. Commun. 8 (1) (2017) 16107, https://doi.org/10.1038/ncomms16107.
[46] B. Martin, W.S. Fyfe, Some experimental and theoretical observations on the kinetics of hydration reactions with particular reference to serpentinization, Chem. Geol. 6 (1970) 185–202, https://doi.org/10.1016/0009-2541(70)90018-5.
[47] T.M. McCollom, F. Klein, M. Robbins, B. Moskowitz, T.S. Berquó, N. Jöns, W. Bach, A. Templeton, Temperature trends for reaction rates, hydrogen generation, and partitioning of iron during experimental serpentinization of olivine, Geochim. Cosmochim. Acta 181 (2016) 175–200, https://doi.org/10.1016/j.gca.2016.03.002.
[48] Y. Ogasawara, A. Okamoto, N. Hirano, N. Tsuchiya, Coupled reactions and silica diffusion during serpentinization, Geochim. Cosmochim. Acta 119 (2013) 212–230, https://doi.org/10.1016/j.gca.2013.06.001.
[49] M. Pens, M. Andreani, I. Daniel, J.-P. Perrillat, H. Cardon, Contrasted effect of aluminum on the serpentinization rate of olivine and orthopyroxene under hydrothermal conditions, Chem. Geol. 441 (2016) 256–264, https://doi.org/10.1016/j.chemgeo.2016.08.007.
[50] W.E. Seyfried, D.I. Foustoukos, Q. Fu, Redox evolution and mass transfer during serpentinization: an experimental and theoretical study at 200°C, 500bar with implications for ultramafic-hosted hydrothermal systems at Mid-Ocean ridges, Geochim. Cosmochim. Acta 71 (15) (2007) 3872–3886, https://doi.org/10.1016/j.gca.2007.05.015.
[51] W.W. Wegner, W. Ernst, Experimentally determined hydration and dehydration reaction rates in the system $MgO\text{-}SiO_2\text{-}H_2O$, Am. J. Sci. 283 (1983) 151–180.
[52] C. Marcaillou, M. Muñoz, O. Vidal, T. Parra, M. Harfouche, Mineralogical evidence for H2 degassing during serpentinization at 300°C/300bar, Earth Planet. Sci. Lett. 303 (3) (2011) 281–290, https://doi.org/10.1016/j.epsl.2011.01.006.
[53] B. Malvoisin, F. Brunet, Water diffusion-transport in a synthetic dunite: consequences for oceanic peridotite serpentinization, Earth Planet. Sci. Lett. 403 (2014) 263–272, https://doi.org/10.1016/j.epsl.2014.07.004.
[54] A. Neubeck, N.T. Duc, D. Bastviken, P. Crill, N.G. Holm, Formation of H_2 and CH_4 by weathering of olivine at temperatures between 30 and 70°C, Geochem. Trans. 12 (1) (2011) 6, https://doi.org/10.1186/1467-4866-12-6.
[55] E.T. Ellison, A.S. Templeton, S.D. Zeigler, L.E. Mayhew, P.B. Kelemen, J.M. Matter, P., The Oman drilling project science, low-temperature hydrogen formation during aqueous alteration of serpentinized peridotite in the Samail ophiolite, J. Geophys. Res. Solid Earth 126 (6) (2021) e2021JB021981, https://doi.org/10.1029/2021JB021981.
[56] A.M. Jones, P.J. Griffin, R.N. Collins, T.D. Waite, Ferrous iron oxidation under acidic conditions – the effect of ferric oxide surfaces, Geochim. Cosmochim. Acta 145 (2014) 1–12, https://doi.org/10.1016/j.gca.2014.09.020.
[57] K. Kanie, A. Muramatsu, S. Suzuki, Y. Waseda, Influence of sulfate ions on conversion of $Fe(OH)_3$ gel to β-FeOOH and $\alpha\text{-}Fe_2O_3$, Mater. Trans. 45 (3) (2004) 968–971, https://doi.org/10.2320/matertrans.45.968.
[58] S.-K. Kwon, K.i. Kimijima, K. Kanie, A. Muramatsu, S. Suzuki, E. Matsubara, Suppression of the conversion process of $Fe(OH)_3$ to β-FeOOH and $\alpha\text{-}Fe_2O_3$ by silicate ions 24 (5) (2005) 275–288, https://doi.org/10.1515/HTMP.2005.24.5.275.
[59] T. Sugimoto, M.M. Khan, A. Muramatsu, H. Itoh, Formation mechanism of monodisperse peanut-type $\alpha\text{-}Fe_2O_3$ particles from condensed ferric hydroxide gel, Colloids Surf. A Physicochem. Eng. Asp. 79 (2) (1993) 233–247, https://doi.org/10.1016/0927-7757(93)80178-H.
[60] T. Sugimoto, K. Sakata, A. Muramatsu, Formation mechanism of monodisperse Pseudocubic $\alpha\text{-}Fe_2O_3$ particles from condensed ferric hydroxide gel, J. Colloid Interface Sci. 159 (2) (1993) 372–382, https://doi.org/10.1006/jcis.1993.1336.
[61] T. Sugimoto, Y. Wang, H. Itoh, A. Muramatsu, Systematic control of size, shape and internal structure of monodisperse $\alpha\text{-}Fe_2O_3$ particles, Colloids Surf. A Physicochem. Eng. Asp. 134 (3) (1998) 265–279, https://doi.org/10.1016/S0927-7757(97)00103-9.
[62] P. Han, D.M. Bartels, Temperature dependence of oxygen diffusion in H_2O and D_2O, J. Phys. Chem. 100 (13) (1996) 5597–5602, https://doi.org/10.1021/jp952903y.
[63] D.T. Kallikragas, A.Y. Plugatyr, I.M. Svishchev, High temperature diffusion coefficients for O_2, H_2, and OH in water, and for pure water, J. Chem. Eng. Data 59 (6) (2014) 1964–1969, https://doi.org/10.1021/je500096r.
[64] S.H. Lee, J.C. Rasaiah, Proton transfer and the mobilities of the H^+ and OH^- ions from studies of a dissociating model for water, J. Chem. Phys. 135 (12) (2011) 124505, https://doi.org/10.1063/1.3632990.
[65] G.K.H. Wiberg, M. Arenz, On the influence of hydronium and hydroxide ion diffusion on the hydrogen and oxygen evolution reactions in aqueous media, Electrochim. Acta 159 (2015) 66–70, https://doi.org/10.1016/j.electacta.2015.01.098.
[66] L. Yuan-Hui, S. Gregory, Diffusion of ions in sea water and in deep-sea sediments, Geochim. Cosmochim. Acta 38 (5) (1974) 703–714, https://doi.org/10.1016/0016-7037(74)90145-8.
[67] D. Kashchiev, Chapter 2 - driving force for nucleation, in: D. Kashchiev (Ed.), Nucleation, Butterworth-Heinemann, Oxford, 2000, pp. 9–16, https://doi.org/10.1016/B978-075064682-6/50003-2.
[68] D. Kashchiev, Chapter 3 - work for cluster formation, in: D. Kashchiev (Ed.), Nucleation, Butterworth-Heinemann, Oxford, 2000, pp. 17–44, https://doi.org/10.1016/B978-075064682-6/50004-4.
[69] D. Kashchiev, Chapter 4 - nucleus size and nucleation work, in: D. Kashchiev (Ed.), Nucleation, Butterworth-Heinemann, Oxford, 2000, pp. 45–57, https://doi.org/10.1016/B978-075064682-6/50005-6.
[70] D. Kashchiev, Chapter 5 - nucleation theorem, in: D. Kashchiev (Ed.), Nucleation, Butterworth-Heinemann, Oxford, 2000, pp. 58–69, https://doi.org/10.1016/B978-075064682-6/50006-8.
[71] J.R. Espinosa, C. Vega, C. Valeriani, D. Frenkel, E. Sanz, Heterogeneous versus homogeneous crystal nucleation of hard spheres, Soft Matter 15 (47) (2019) 9625–9631, https://doi.org/10.1039/C9SM01142K.
[72] K.F. Kelton, Crystal nucleation in liquids and glasses, in: H. Ehrenreich, D. Turnbull (Eds.), Solid State Physics, Academic Press, 1991, pp. 75–177, https://doi.org/10.1016/S0081-1947(08)60144-7.

[73] S.L. Brantley, J.D. Kubicki, A.F. White, Kinetics of Water-Rock Interaction, Springer Link, 2008, https://doi.org/10.1007/978-0-387-73563-4.
[74] H.E. King, O. Plümper, A. Putnis, Effect of secondary phase formation on the carbonation of olivine, Environ. Sci. Technol. 44 (16) (2010) 6503–6509, https://doi.org/10.1021/es9038193.
[75] O. Sissmann, D. Daval, F. Brunet, F. Guyot, A. Verlaguet, Y. Pinquier, N. Findling, I. Martinez, The deleterious effect of secondary phases on olivine carbonation yield: insight from time-resolved aqueous-fluid sampling and FIB-TEM characterization, Chem. Geol. 357 (2013) 186–202, https://doi.org/10.1016/j.chemgeo.2013.08.031.
[76] G.D. Saldi, D. Daval, G. Morvan, K.G. Knauss, The role of Fe and redox conditions in olivine carbonation rates: an experimental study of the rate limiting reactions at 90 and 150°C in open and closed systems, Geochim. Cosmochim. Acta 118 (2013) 157–183, https://doi.org/10.1016/j.gca.2013.04.029.
[77] G.D. Saldi, D. Daval, H. Guo, F. Guyot, S. Bernard, C.L. Guillou, J.A. Davis, K. G. Knauss, Mineralogical evolution of Fe–Si-rich layers at the olivine-water interface during carbonation reactions 100 (11−12) (2015) 2655–2669, https://doi.org/10.2138/am-2015-5340.
[78] R.C.L. Jonckbloedt, Olivine dissolution in sulphuric acid at elevated temperatures—implications for the olivine process, an alternative waste acid neutralizing process, J. Geochem. Explor. 62 (1) (1998) 337–346, https://doi.org/10.1016/S0375-6742(98)00002-8.
[79] V.A. Alekseyev, L.S. Medvedeva, N.I. Prisyagina, S.S. Meshalkin, A.I. Balabin, Change in the dissolution rates of alkali feldspars as a result of secondary mineral precipitation and approach to equilibrium, Geochim. Cosmochim. Acta 61 (6) (1997) 1125–1142, https://doi.org/10.1016/S0016-7037(96)00405-X.
[80] E.H. Oelkers, J. Schott, J.-L. Devidal, The effect of aluminum, pH, and chemical affinity on the rates of aluminosilicate dissolution reactions, Geochim. Cosmochim. Acta 58 (9) (1994) 2011–2024, https://doi.org/10.1016/0016-7037(94)90281-X.
[81] A.C. Lasaga, Chapter 2. Fundamental approaches in describing mineral dissolution and precipitation rates, in: A.F. White, S.L. Brantley (Eds.), Chemical Weathering Rates of Silicate Minerals, De Gruyter, 1995, pp. 23–86, https://doi.org/10.1515/9781501509650-004.
[82] A.C. Lasaga, Princeton University Press, Princeton, 2014. doi:doi:https://doi.org/10.1515/9781400864874.
[83] A.C. Lasaga, J.M. Soler, J. Ganor, T.E. Burch, K.L. Nagy, Chemical weathering rate laws and global geochemical cycles, Geochim. Cosmochim. Acta 58 (10) (1994) 2361–2386, https://doi.org/10.1016/0016-7037(94)90016-7.